Quantum Acoustics with Tunable Nonlinearity in the Superstrong Coupling Regime

Marco Scigliuzzo,[1,2,3,*] Léo Peyruchat,[4,1,*] Riccardo Maria Marabini,[4,1] Carla Becker,[4,1] Vincent Jouanny,[4,1] Per Delsing,[3,†] and Pasquale Scarlino[4,1,‡]

[1] *Center for Quantum Science and Engineering, École Polytechnique Fédérale de Lausanne (EPFL), Lausanne CH-1015, Switzerland*

[2] *Laboratory of Photonics and Quantum Measurements (LPQM), Institute of Physics, EPFL, Lausanne CH-1015, Switzerland*

[3] *Department of Microtechnology and Nanoscience, Chalmers University of Technology, Gothenburg 412 96, Sweden*

[4] *Hybrid Quantum Circuits Laboratory (HQC), Institute of Physics, École Polytechnique Fédérale de Lausanne (EPFL), Lausanne 1015, Switzerland*

(Received 24 June 2025; revised 29 December 2025; accepted 9 January 2026; published 24 March 2026)

Precise control of mechanical modes in the quantum regime is a key resource for quantum technologies, offering promising pathways for quantum sensing with macroscopic systems and scalable architectures for quantum simulation. In this work, we realize a multimode mechanical cavity coupled to a superconducting Kerr resonator, which induces nonlinearity in the mechanical modes. The Kerr mode is realized by a flux-tunable superconducting quantum interference device (SQUID) array resonator, while the mechanical modes are implemented by a surface acoustic wave cavity. Both mechanical and electromagnetic modes are individually addressable via dedicated measurement lines, enabling full spectroscopic characterization. We introduce a straightforward protocol to measure the SQUID array resonator's participation ratio in the hybrid acoustic modes, quantifying the degree of hybridization. The participation ratio reveals that our device operates at the onset of the multimode coupling regime, where multiple acoustic modes simultaneously interact with the nonlinear superconducting element. Furthermore, this platform allows controllable Kerr-type nonlinearities in multiple acoustic modes, with the participation ratio serving as the key parameter determining both the dissipation rates and nonlinear strengths of these hybridized modes. Close to the resonant regime, we measure a cross-Kerr interaction between seven pairs of mechanical modes, which is controllable via the SQUID array resonator detuning. Finally, we apply a two-photon parametric drive to the SQUID array resonator and observe the resulting parametric down-conversion and metastable state switching in a mechanical mode. These results establish a platform for engineering nonlinear multimode mechanical interactions, offering potential for future integration with superconducting qubits and implementation of multiple mechanical qubits.

DOI: 10.1103/rk3m-dnwp

I. INTRODUCTION

Developing the quantum control of mechanical modes represents a fundamental task for quantum science and technologies. Due to their mass, mechanical systems possess distinctive properties, such as sensitivity to weak external forces, acceleration, and even gravitational effects [1,2]. Moreover, the slow propagation speed of mechanical excitations results in a reduced footprint for the mechanical system and enables exploration of exotic interaction regimes, such as the "giant atom" limit [3,4].

Over the past two decades, significant advances have established the field of quantum acoustics [5,6], with a wide range of hybrid platforms developed to interface mechanical degrees of freedom with quantum systems. These include levitated particles [7], cold atoms [8], and a variety of solid-state systems [9]. Among these, solid-state mechanical platforms stand out by leveraging superconducting circuit technologies and lithographically defined mechanical elements, such as phononic crystal defects [10], membranes [11,12], bulk acoustic

*These two authors contributed equally.
†Contact author: per.delsing@chalmers.se
‡Contact author: pasquale.scarlino@epfl.ch

Published by the American Physical Society under the terms of the Creative Commons Attribution 4.0 International license. Further distribution of this work must maintain attribution to the author(s) and the published article's title, journal citation, and DOI.

resonators [13], and surface acoustic wave (SAW) devices [3,14–19].

These systems have enabled precise quantum control of single mechanical modes. A common approach is to prepare a high-fidelity quantum state in a superconducting qubit and transfer the excitation to a mechanical mode, enabling squeezed states [20,21], Fock states [22,23], and other nonclassical states [24]. An alternative approach is to introduce nonlinearity into mechanical modes [21,25–30], which can mediate interactions between mechanical modes. Despite these advances, progress has largely remained confined to single-mode systems. Although recent works have demonstrated quantum operations on multiple mechanical modes, including two-mode entanglement [31] and three-mode beamsplitter coupling [32], scaling to quantum control across larger multimode systems remains challenging.

In this context, SAW resonators offer a distinct advantage: their acoustic mode confinement is restricted to a well-defined frequency band. As a result, electromagnetic resonators or qubits can be tuned outside this range without interacting with the SAW modes, enabling greater flexibility in device design. This frequency stop band is lithographically defined by the Bragg gratings during fabrication [33]. The multimode nature of SAW resonators has been leveraged to probe high-density ensembles of surface two-level systems (TLSs) [34,35], providing a valuable tool for material and interface characterization. In addition, SAW devices are highly versatile and readily integrable with a broad range of platforms, including optical cavities [36], photonic waveguides [37], and even propagating optical photons [38]. Their compatibility extends further to solid-state quantum systems, having been successfully coupled to vacancy centers in various substrates [39,40] and to electrically defined semiconductor qubits [41,42].

In this work, we investigate the onset of the multimode (i.e., superstrong) coupling regime [43–47] between mechanical modes of a SAW cavity and a flux-tunable, nonlinear electromagnetic ancilla [10,48,49]. The system consists of 29 mechanical modes with distinct frequencies ω_i, each coupled to the fundamental mode of a superconducting superconducting quantum interference device (SQUID) array resonator, whose frequency ω_{SQ} can be tuned in situ via external magnetic flux. In contrast to the strong nonlinearity of transmon qubits employed in related multimode systems [21,32,45,50], we use a SQUID array [10,48,49] as a moderately nonlinear ancilla with reduced Kerr interaction. This design choice offers advantages for systematic characterization of multimode nonlinear phenomena. The moderate nonlinearity suppresses higher-order processes, extending the dynamic range of parametric operations [28,51,52], and enables larger photon populations for enhanced signal-to-noise ratio in device characterization. Despite this reduced nonlinearity, the Kerr interaction remains comparable to dissipation rates, sufficient to observe dissipative phase transitions [53,54] with potential applications in quantum sensing [55,56]. The platform further supports controllable mode conversion between mechanical modes via parametric coupling [32,57,58].

We begin by performing single-tone spectroscopy to establish the multimode coupling regime, characterized by the condition where the mechanical mode frequency spacing [free spectral range (FSR), $\Delta\omega_i$] becomes comparable to the individual coupling strengths g_i between the electromagnetic and mechanical modes. To quantify the hybridization between the electromagnetic and mechanical degrees of freedom, we introduce a participation-ratio metric based on the relative frequency shifts of the mechanical modes as a function of the SQUID array resonator detuning. This metric enables accurate prediction of both the dissipation and nonlinear response of the hybridized modes. We further experimentally observe and characterize cross-Kerr interactions χ_{ij} among seven distinct acoustic modes, demonstrating the emergence of nonlinear interactions mediated by the shared coupling to the nonlinear electromagnetic ancilla. These results confirm the nonlinear multimode character of the system and validate the participation-based model. We exploit the mechanical nonlinearity to activate multiphoton effects. By applying a parametric drive on the flux line of the SQUID array, and collecting the output field from the SAW resonator port, we measure parametric down-conversion and switching between mechanical metastable states.

Finally, we discuss how this platform can be extended toward implementing multiple mechanical qubits [29]. This device and these measurement techniques represent a step toward full multimode quantum control, which will allow the generation of large multimode quantum states with a single gate.

II. RESULTS

A. Setup and device

1. Device

The device presented in Fig. 1 features a nonlinear electromagnetic resonator coupled to a linear multimode mechanical cavity. The electromagnetic resonator is implemented as an interdigital capacitor shunted by an array of $N_{\mathrm{s}} = 12$ SQUIDs. The frequency $\omega_{\mathrm{SQ}}(\phi_X)$ of the fundamental mode $\hat{a}$ can be tuned by threading magnetic flux ϕ_X through each SQUID loop. The additional $N_{\mathrm{s}} - 1$ modes have a much higher frequency, and they do not impact the physics investigated in this work. The mechanical modes $\hat{b}_i$ are SAWs confined between two Bragg mirrors and directly excited or detected by an interdigital transducer (launcher IDT). The coupling between the electromagnetic

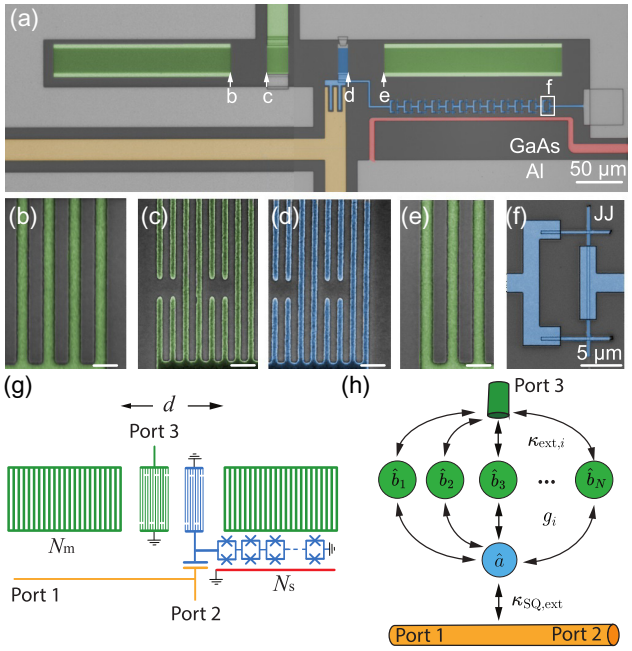


FIG. 1. Surface acoustic wave cavity coupled to a SQUID array resonator. (a) False color optical image of the device. (b) and (e) Two Bragg mirrors form an acoustic cavity. (c) A large launcher interdigital transducer with 30 pairs of split fingers is coupled to a microwave feedline to probe surface acoustic wave modes in reflection. (d) A SQUID array forms a nonlinear $\lambda/4$ resonator with a shunt to ground on the right side, and a capacitive end on the left side which is connected to a microwave feedline in notch configuration (yellow) and to surface acoustic wave modes via a smaller coupler interdigital transducer with 14 pairs of split fingers. A flux line (red) enables uniform flux threading. (f) SEM micrograph showing an enlargement of the highlighted white rectangle in panel (a), reporting a zoom-in of a single SQUID. (g) Circuit schematic of the systems. The mirrors are separated by $d = 155\,\mu$m and both present a Bragg grating with $N_m = 500$ finger elements, much longer than the penetration length. The SQUID array resonator features $N_s = 12$ SQUID units. (h) Mode diagram representing the surface acoustic wave cavity modes, $\hat{b}_i$, coupled to the SQUID array resonator mode, $\hat{a}$, together with their respective external dissipation rates, $\kappa_{\mathrm{ext},i}$ and $\kappa_{\mathrm{SQ,ext}}$.

and mechanical excitations is implemented by an interdigital transducer at the capacitive end of the SQUID array resonator (coupler IDT).

The SAW components are designed for wavelength $\lambda_0 = 720$ nm. A Bragg mirror consists of $N_{\mathrm{m}} = 500$ fingers 180 nm wide realized with 30 nm thin aluminum films [see Figs. 1(b) and 1(e)] that yield ≈ 100 MHz wide stopband around the frequency $v_{\mathrm{SAW}}/\lambda_0 \approx 4$ GHz. The distance between the mirrors is $d = 155\,\mu$m. Both the launcher and coupler IDTs [see Figs. 1(c) and 1(d) respectively] are realized with split-finger geometry to prevent internal reflection within the mirror [59], and they have 30 and 14 pairs of split fingers, respectively.

The sample is bonded on a PCB, enclosed in a tri-layer Cu-Al-μ-metal shield, mechanically and thermally anchored at the mixing chamber plate of a dilution refrigerator with base temperature of 10 mK (see Sec C 2 for more information).

As depicted in the circuit schematic of Fig. 1(g), the resonator is coupled to the microwave feedline in a notch configuration and can be measured via ports 1 and 2; similarly, the SAW modes can be directly excited and measured in reflection from port 3. The mode diagram is finally reported in Fig. 1(h). Throughout the article, we use blue colors for S_{21} and green for S_{33} scattering coefficients.

B. Bare elements

The Hamiltonian of the device in the bare mode basis is

$$H/\hbar = \omega_{\mathrm{SQ}}(\phi_X)\, a^\dagger a + \chi_{\mathrm{SQ}}(a^\dagger a)^2 + \sum_{i=1}^{29} \omega_i\, b_i^\dagger b_i + \sum_{i=1}^{29} g_i (a^\dagger b_i + a b_i^\dagger), \quad (1)$$

where χ_{SQ} is the SQUID array resonator nonlinearity, ω_i is the resonance frequency of the ith SAW cavity mode, and g_i the coupling between ith SAW cavity and SQUID array resonator [see Fig. 1(h)].

1. Bare SAW modes

We first characterize the bare SAW modes. The SQUID array resonator is set to $\omega_{\mathrm{SQ}}(0)/2\pi \approx 4.7$ GHz, corresponding to detuning of 700 MHz from the central frequency of the SAW cavity. We then measure S_{33}, as shown in Fig. 2(a), and normalize the data by dividing out the slowly varying background of S_{33}. We observe SAW modes from 3.93 GHz to 4.05 GHz. Modes with higher visibility correspond to longitudinal excitations. They are indexed by odd numbers and have a free spectral range of approximately 8.6 MHz [59]. Each longitudinal mode is accompanied by a transverse mode with weaker visibility detuned by roughly 2 MHz to a higher frequency [60]. We label these with even indices. Finite element simulations of both longitudinal and transverse modes, shown in Fig. 16, confirm this identification.

The dissipation rates of each resolved SAW mode are obtained by fitting Eq. (B19) and are reported in Figs. 2(b) and 2(c). The longitudinal SAW modes are undercoupled to the launcher IDT, with an approximately constant internal dissipation rate $\kappa_{\mathrm{int}}/2\pi \approx 80$ kHz across modes. The maximum external coupling $\kappa_{\mathrm{ext}}/2\pi \approx 31$ kHz is achieved for mode 11 near the center of the mirror bandwidth. Transverse SAW modes are weakly coupled to the launcher IDT ($\kappa_{\mathrm{ext}}/2\pi < 5$ kHz) and have larger internal losses ($\kappa_{\mathrm{int}}/2\pi \approx 315$ kHz). The measurement is

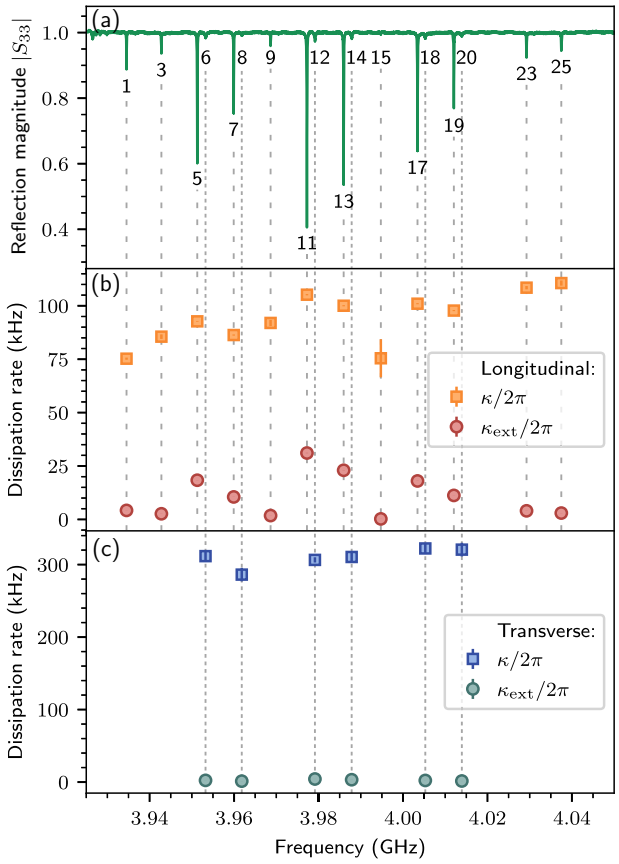


FIG. 2. Bare surface acoustic wave modes. (a) Reflection magnitude $|S_{33}|$ measured from the surface acoustic wave launcher interdigital transducer feedline. Dashed lines mark the longitudinal modes (odd indices), while dotted lines mark six resolved transverse modes (even indices). (b) Extracted dissipation rates of longitudinal surface acoustic wave modes, which are undercoupled: the total dissipation rate (squares) exceeds twice the external rate (circles). (c) Dissipation rates of transverse surface acoustic wave modes, which exhibit smaller external coupling and larger internal dissipation than the longitudinal modes. We used a probe power of −131 dBm at the device input, corresponding to an average phonon occupancy of 23 for the longitudinal modes. Error bars are obtained from fits and represent one standard deviation.

performed with −131 dBm input power at the device level, leading to an average occupation of 23 phonons (see Eq. (B20) for calibration). For a more general characterization of the dissipation rates as a function of probe power, see Fig. 17 in the Appendix. Due to the spatial profile of the mechanical modes, some modes are weakly coupled to the launcher IDT (e.g., mode 21 expected at 4.02 GHz) [16].

2. Bare SQUID array resonator

We now characterize the bare SQUID array resonator. In Fig. 3(a), we measure the transmission S_{21} of the waveguide (see Fig. 1) while sweeping the flux in the SQUIDs by threading current in an external superconducting coil. The transmission data is normalized by a background trace measured with the SQUID array tuned at low frequency (near half flux quanta). We extract the SQUID array resonator frequency and fit it to Eq. (B17) to convert applied current in the external coil to bare SQUID array resonator frequency ω_{SQ}.

The external coupling rate $\kappa_{\mathrm{SQ,ext}}$ to the feedline scales with ω_{SQ}^2, and remains in the range 4-6 MHz (see the fit to Fig. 18 in the Appendix). The internal dissipation rate at single photon is limited by the electric field participation ratio in the launcher IDT, except in the frequency region approximately 300 MHz-wide where the IDT coupler emits SAWs (see Sec. D 2 b for more details).

The direct coupling from the SQUID feedline to SAW modes via the coupler IDT is negligible, with external coupling rates below 0.4 kHz.

C. SAW-SQUID hybridization

1. Flux sweep and resonant coupling

In Figs. 3(b) and 3(c), we report a detailed sweep of the flux in the range where the bare SQUID array resonator frequency is within the SAW mirror stopband, and measure the response of the SQUID array resonator mode $\hat{a}$ (S_{21}), and the SAW modes $\hat{b}_i$ (S_{33}), respectively. The extinction rates of these resonances differ in the two measurements due to different coupling to the relative excitation ports (notice that the color bar legend shows different amplitudes for each panel).

Combining the information in panels (b) and (c), we count 29 SAW modes. However, in the characterization shown in Fig. 2, we only found the frequency of 12 longitudinal modes and 6 transverse SAW modes. Therefore, we fit the detailed flux sweeps to the linear part of Hamiltonian in Eq. (1) with the frequency of the 11 missing SAW modes and all the 29 g_i couplings as free parameters. The couplings g_i are different for each SAW mode due to the different overlap of their mode shape with coupler IDT; the values obtained from the fit are shown in Fig. 3(d). The coupling to transverse SAW modes is about three times weaker than to longitudinal modes due to lower overlap with the coupler IDT.

The frequency difference $\Delta\omega_i = \omega_{i+1} - \omega_i$ between SAW modes alternates between approximately 2.0 and 6.5 MHz in $\Delta\omega_i/2\pi$, as shown in Fig. 15. The couplings g_i are comparable to these local spacings, with averages $g_{\mathrm{longitudinal}}/2\pi \approx 3.8$ MHz and $g_{\mathrm{transverse}}/2\pi \approx 1.4$ MHz (averaged over all SAW-SQUID couplings, including modes with suppressed overlap). The conventional criterion for the multimode (or superstrong) coupling regime, $g \gtrsim \Delta\omega$, is typically formulated for uniform spectra with nearly equispaced modes and weakly mode-dependent coupling [43–47]. Because our device

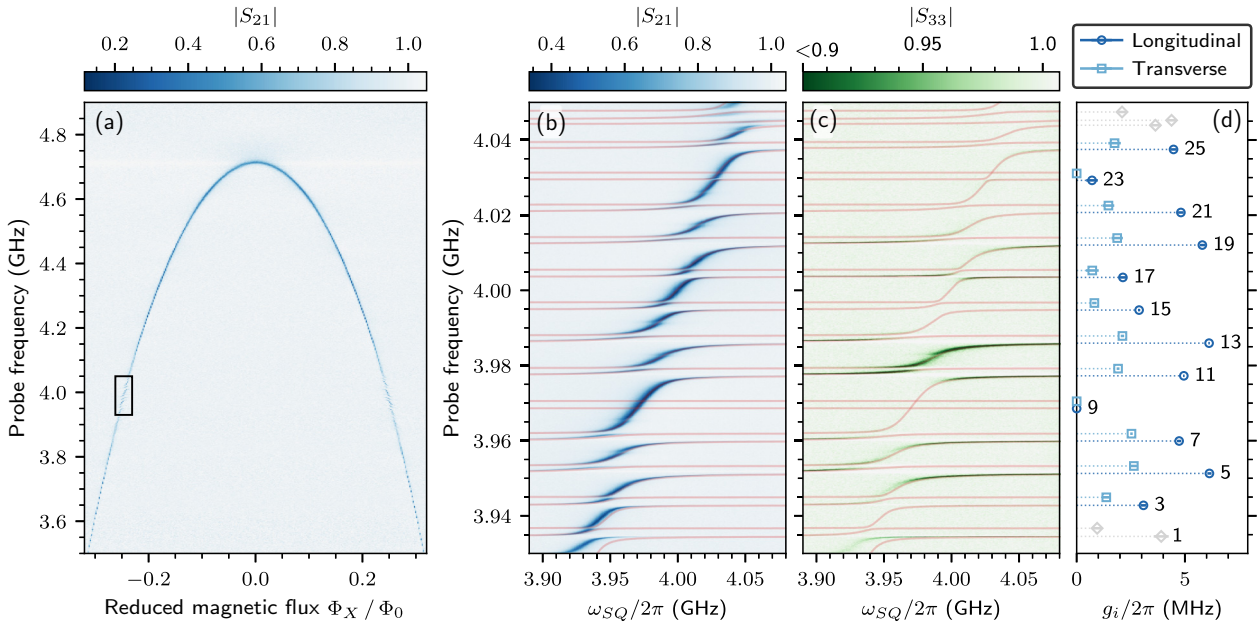


FIG. 3. Flux sweep of the SQUID array resonator across surface acoustic wave modes. (a) Normalized transmission S_{21} through the SQUID array resonator feedline, measured as a function of flux threading the SQUID array generated by an external coil. The power of the probe tone is −142 dBm. (b) and (c) Magnitude of S_{21} (blue) and S_{33} (green) measured as a function of flux sweeps across the surface acoustic wave modes in the region highlighted by the black rectangle in panel (a). The power of the probe tone applied to port 1 is −132 dBm, while the power of the probe tone applied to port 3 is −131 dBm. The peak position obtained from a multimode fit is shown with red solid lines and is in excellent agreement with the experimental data except for the modes at the edge of the mirror bandwidth [gray in (d)]. (d) Coupling rates between the electromagnetic and mechanical modes, g_i, extracted from the multimode fit. The couplings to longitudinal surface acoustic wave modes are shown with dark blue circle markers, while the couplings to transverse surface acoustic wave modes are shown with light blue square markers. Error bars are obtained from the fit and represent one standard deviation.

exhibits uneven mode spacing and mode-dependent couplings g_i, this uniform-cavity criterion is not directly applicable. Instead, we quantify the multimode regime using local, mode-resolved coupling-to-spacing ratios defined in Sec. D 3 and plotted in Fig. 19. Using these metrics, a subset of modes have ratios exceeding unity, while the average ratio over all modes is just below one (typical values 0.6–0.9, depending on the metric). We therefore describe the device as operating at the onset of the multimode (or superstrong) coupling regime, the consequence of which we will study in the rest of the article.

2. Model in hybridized mode basis

To study the system in the resonant regime of mechanical and electromagnetic modes ($\omega_{\mathrm{SQ}} \approx \omega_i$), it is convenient to rewrite the Hamiltonian from Eq. (1) in the basis of hybridized modes. As detailed in Sec. B 1 a, we apply a Bogoliubov transformation [61] to the linear part of the Hamiltonian and expand the Kerr term perturbatively to obtain

$$\tilde{H}/\hbar = \sum_{i=0}^{29} \tilde{\omega}_i\, c_i^\dagger c_i + \sum_{i,j=0}^{29} \tilde{\chi}_{ij}\, c_i^\dagger c_j^\dagger c_i c_j\,. \tag{2}$$

All the hybridized modes c_i now have self-Kerr $\tilde{\chi}_{i,i}$ and cross-Kerr $\tilde{\chi}_{i\neq j}$ nonlinearities. The hybridized modes c_i can be decomposed in the bare mode basis as

$$c_j = a\, u_{\mathrm{SQ},j} + \sum_{i=1}^{29} b_i\, u_{i,j}\,, \tag{3}$$

where $u_{i,j}$ corresponds to the coefficients defined in Eq. (B11), and $u_{\mathrm{SQ},j} = u_{0,j}$. As we demonstrate below, the nonlinearities $\tilde{\chi}_{i,j}$ and dissipation rates $\tilde{\kappa}_i$ of the c_i modes can be simply obtained from the participation of the SQUID array resonator $|u_{\mathrm{SQ},i}|^2$.

3. Participation-ratio analysis

The participation ratio of nonlinear circuit elements is a widely used concept for modeling and designing superconducting circuits [62,63]. This method provides an efficient way to analyze systems combining linear and nonlinear elements. Unlike a full quantum simulation of the device, this approach simplifies the problem by first performing a linear simulation to calculate the eigenmodes of the system. The system's couplings and nonlinearities are then determined from the overlap between the eigenmodes and the nonlinear elements.

Here, we propose a simple and accurate method to extract the SQUID array resonator participation directly from measurements of the hybrid mode frequency as a function of the SQUID array resonator frequency. Specifically, we derive in the Appendix [Eq. (B16)] the following relationship:

$$|u_{\mathrm{SQ},i}|^2 = \frac{\mathrm{d}\tilde{\omega}_i}{\mathrm{d}\omega_{\mathrm{SQ}}}. \tag{4}$$

4. Participation-ratio measurement from eigenmode derivative

Two coupled resonant systems hybridize, forming superpositions of the two bare states. However, because our system is in the multimode coupling regime, the bare SQUID array resonator mode $\hat{a}$ hybridizes simultaneously with multiple bare SAW modes $\hat{b}_i$. As a result, the participation of the SQUID array resonator in the hybrid eigenmodes remains small through the avoided crossings. While this feature has been discussed in previous works [45], it has not been explicitly measured. We now apply our proposed method [Eq. (4)] to directly measure the SQUID array resonator participation in hybrid modes c_{11} and c_{12} and verify these predictions.

In Fig. 4, we fit the measurements of the detail ed flux sweeps in panels a and b to the input output model of Eq. (B18) for S_{21} and Eq. (B19) for S_{33}, and obtain the frequencies and dissipation rates of the hybridized modes. We numerically compute the derivative of the measured frequencies as a function of ω_{SQ}. Blue and green markers in panels (c) and (e) show the derivative obtained from the measurement of S_{21} and S_{33}, respectively. We also compute the participation of the bare modes by diagonalizing the linear part of the Hamiltonian Eq. (1) with the parameters of the multimode fit extracted from Figs. 3(b) and 3(c). The solid lines in Figs. 4(c) and 4(e) correspond to bare SAW modes, with the modes participating with less than 2 % shown in gray, and the black dashed line corresponds to $|u_{\mathrm{SQ},i}|^2$. We find an excellent agreement with the measurements, down to $|u_{\mathrm{SQ},i}|^2 \simeq 0.1\,\%$. The hybridized mode c_{12} is at the onset of multimode regime, with a maximum SQUID array resonator participation of 20 %, and four bare SAW modes with participation above 3 %. The hybridized mode c_{11} is deeper in the multimode regime. Indeed, it remains mainly acoustic all across the avoided crossing, with a maximum SQUID array resonator participation of only $|u_{\mathrm{SQ},i}|^2 \simeq 4\,\%$.

5. Participation-dissipation rate

We now focus on how the total dissipation rates $\tilde{\kappa}_j$ of the hybridized modes evolve as a function of the SQUID array resonator frequency ω_{SQ}. As shown in Figs. 4(d) and 4(f), an increase in dissipation rate is observed when the SQUID array resonator has the largest participation in the hybrid mode. The total dissipation rates $\tilde{\kappa}_j$ of the hybrid mode c_j can be approximated from the participation of the bare modes as

$$\tilde{\kappa}_j \approx |u_{\mathrm{SQ},j}|^2\,\kappa_{\mathrm{SQ}} + \sum_{i=1}^{29} |u_{i,j}|^2\,\kappa_i, \tag{5}$$

where κ_{SQ} is the total dissipation rate of the bare SQUID array resonator, and κ_i denotes the dissipation rate of the ith bare SAW mode. As discussed in Sec. D 5, this expression neglects corrections arising from the overlap of the hybrid SAW mode profiles with the launcher IDT, which modify the effective external coupling [64]. The only unknown parameter in Eq. (5) is κ_{SQ}, of which we do not have direct access when ω_{SQ} is within the Bragg mirror bandwidth. We perform a global fit of the dissipation rates $\tilde{\kappa}_j$ for all hybridized modes from c_{10} to c_{15} using Eq. (5). We fix all the participation ratios by diagonalizing the linear part of Hamiltonian Eq. (1) with the parameters from the multimode fit of Fig. 3(d). All the bare SAW dissipation rates used in the estimation are reported in Fig. 14. We obtain $\kappa_{\mathrm{SQ}}/2\pi = (8.7 \pm 0.7)$ MHz.

Measurements of SQUID array resonator participation and dissipation rates for four additional hybridized modes are presented in the Appendix (see Fig. 20), along with further details on the analysis procedure. We note the presence of a few weakly coupled spurious modes, which may be attributed to higher-order transverse SAW modes. These spurious modes are included in the extended analysis presented in Fig. 21.

Remarkably, although the system operates in the weak-coupling regime at the level of individual SAW modes, characterized by $g_i < \kappa_{\mathrm{SQ}}$, we observe hallmark signatures of strong coupling, such as vacuum Rabi splitting [65] [see Fig. 4(a)]. This behavior arises because the dissipation of the SQUID array resonator is effectively distributed among the many mechanical modes to which it is simultaneously coupled. As a result, an *effective strong coupling* emerges despite each mechanical mode being individually in the weak interaction regime with the SQUID array resonator.

D. Cross-Kerr nonlinearities

1. Participation ratio and nonlinearity-theory

While the dissipation rate $\tilde{\kappa}_i$ of hybridized modes depends linearly on the participation ratio of the bare SQUID array resonator mode [Eq. (5)], the nonlinear interaction terms $\tilde{\chi}_{i,j}$ exhibit a quadratic dependence, as derived in Sec. B 1 a [62],

$$\tilde{\chi}_{i,i} = \chi_{\mathrm{SQ}}\,|u_{\mathrm{SQ},i}|^2\,|u_{\mathrm{SQ},i}|^2, \tag{6a}$$

$$\tilde{\chi}_{i,j} = -2\sqrt{\tilde{\chi}_{i,i}\,\tilde{\chi}_{j,j}} = 2\chi_{\mathrm{SQ}}\,|u_{\mathrm{SQ},i}|^2\,|u_{\mathrm{SQ},j}|^2, \tag{6b}$$

where $i \neq j$.

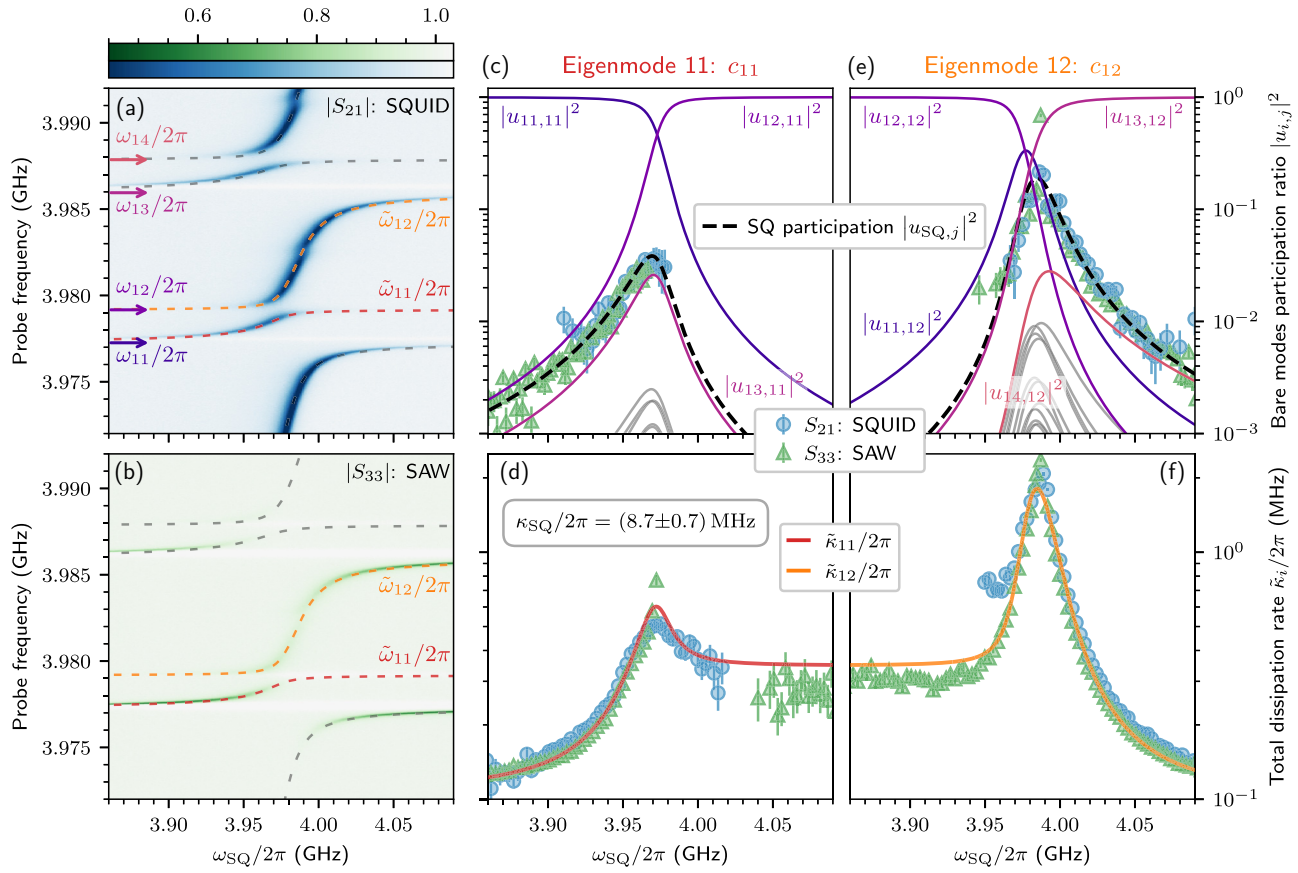


FIG. 4. Characterization of the multimode coupling regime. (a) and (b) Enlarged view of the magnitude of S_{21} (blue) and S_{33} (green), as shown in Figs. 3(b) and 3(c), highlighting four selected surface acoustic wave modes. Dashed lines show the extracted hybridized modes position, with eigenmodes 11 and 12 highlighted in red and orange respectively. Horizontal arrows in (a) indicate the frequencies of the bare surface acoustic wave modes participating in the two eigenmodes. (c) and (e) Participation of the bare modes in the eigenmodes c_{11} (c) and c_{12} (e). The values of $|u_{\mathrm{SQ},i}|^2$ obtained from S_{21} are shown with blue circle markers, while those obtained from S_{33} are shown with green triangle markers. The continuous colored lines represent the participation ratios of the bare surface acoustic wave modes, while the black dashed line indicates the participation of the SQUID array resonator mode, computed from numerical diagonalization of the linear Hamiltonian in Eq. (1). Modes with maximum participation larger than 2% are shown in color, while other surface acoustic wave modes with lower participation are shown in gray. (d) and (f) Total dissipation rates of eigenmodes c_{11} (d) and c_{12} (f), extracted by fitting each individual resonance to the input-output relations Eq. (B18) (S_{21}) or Eq. (B19) (S_{33}). The resulting total dissipation rates from S_{21} and S_{33} are shown as blue circles and green triangles, respectively. Solid lines show a global fit to Eq. (5), from which we extract the total dissipation rate of the SQUID array resonator inside the mirror stopband, $\kappa_{\mathrm{SQ}}/2\pi = 8.7 \pm 0.7$ MHz. All marker error bars represent one standard deviation.

Already in the single-mode coupling regime, a large SQUID array resonator participation can result in a significant self-Kerr nonlinearity [29]. However, achieving sizeable cross-Kerr terms requires substantial SQUID array resonator participation across multiple hybridized modes. Therefore, the multimode coupling regime is essential to simultaneously realize large cross-Kerr interactions at a fixed bare SQUID array resonator frequency [47].

2. Participation ratio and nonlinearity-measurements

Measurements of the cross-Kerr nonlinearity between different hybridized modes as a function of the bare SQUID array resonator frequency are presented in Fig. 5. To characterize the cross-Kerr interactions, we sweep a strong pump tone across one hybridized mode, while weakly probing other eigenmodes to detect frequency shifts induced by the pump. We pump the hybridized mode denoted as c_p in Fig. 5(a). This mode spans c_8, c_9 and c_{10} and appears as a single, continuous mode because the coupler IDT is effectively decoupled from the bare SAW modes b_9 and b_{10} ($g_9 \approx g_{10} \approx 0$). We choose to pump c_p because it yields a substantial cross-Kerr signal over a large range of ω_{SQ}. We have also repeated the measurement while pumping other modes and observed similar agreement with the model.

For each pump power, we perform two-tone spectroscopy by sweeping both the pump and probe

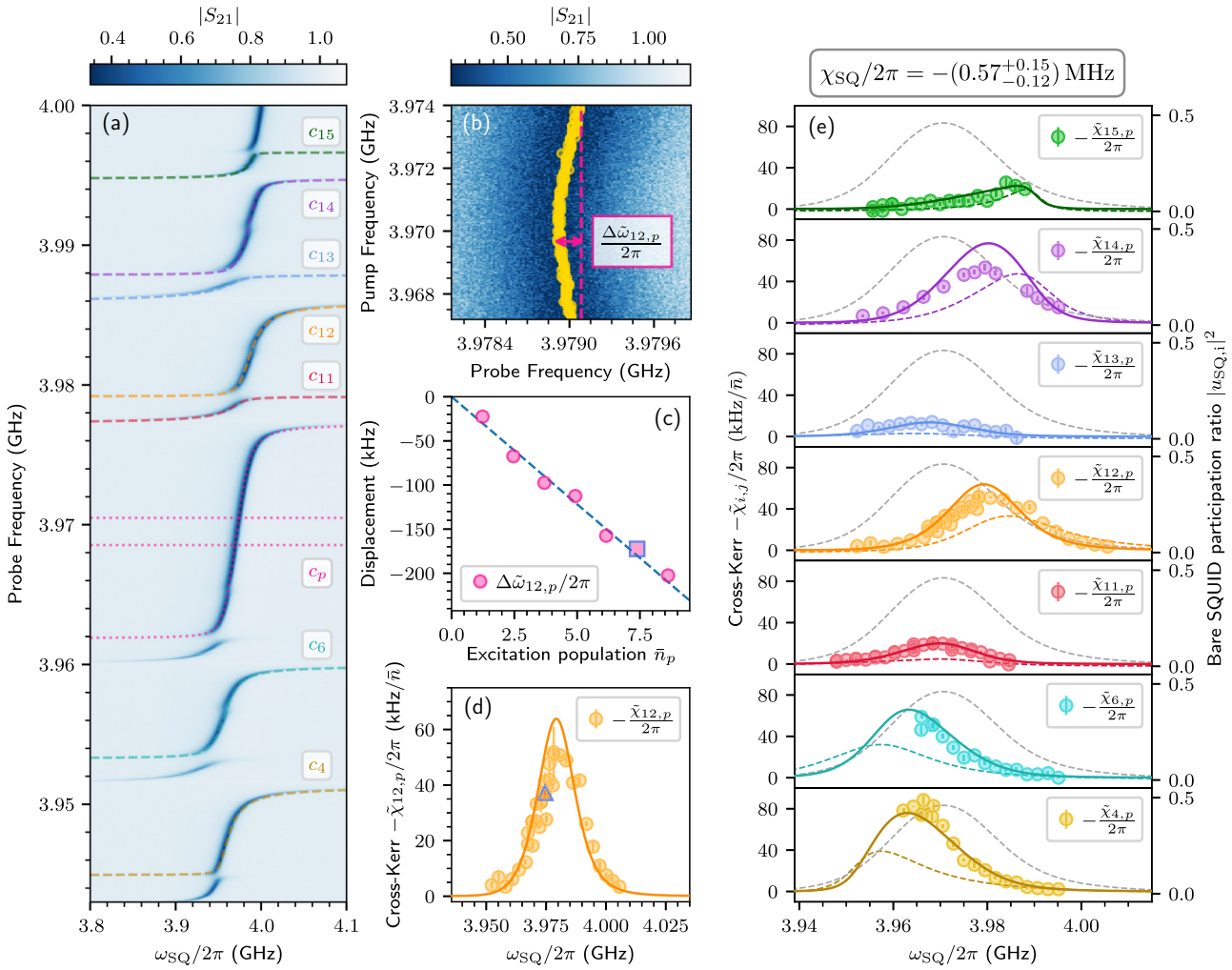


FIG. 5. Cross-Kerr measurement versus bare SQUID array resonator frequency. (a) Normalized transmission S_{21} through the SQUID array resonator feedline, measured as a function of flux threading the SQUID array focusing on modes from c_4 to c_{15}. Dotted pink lines indicate the pumped mode $c_p \in [c_8,\ c_{10}]$, while all the dashed lines represent all the probed modes. (b)–(d) Measurement protocol showing as an example $\tilde{\chi}_{12,p}$ the cross-Kerr between modes c_p and c_{12}. (b) We sweep the frequency across both the pumped mode (c_p) and the probed mode (c_{12}) to find the maximum frequency shift $\Delta f_{12,p}$. (c) We repeat this measurement for increasing pump power, and extract $\tilde{\chi}_{12,p}$ from a linear fit to the displacement against number of excitations in the pumped mode, $\bar{n}_p$. The square marker corresponds to the pump power used in (b). (d) We repeat the protocol outlined in (b) and (c) for different bare SQUID array resonator frequencies ω_{SQ}. The cross-Kerr value extracted in (c) is highlighted with a blue triangle marker. (e) Cross-Kerr as a function of ω_{SQ}, measured while pumping mode c_p, and probing seven different modes, using the same color coding as in panel (a). A global fit of all cross-Kerr data is performed (solid colored lines), with the only free fitting parameter being the bare SQUID Kerr nonlinearity, yielding $\chi_{SQ}/2\pi = 0.57^{+0.15}_{-0.12}$ MHz. The dashed lines in (e) show the bare SQUID participation ratio obtained from the linear model: the gray curve corresponds to the pumped mode, while the colored curves correspond to the probed modes. Error bars on markers in (d) and (e) are obtained from the linear fit of displacements $\Delta\tilde{\omega}_{i,p}$.

frequencies, yielding a map of the mode response as shown in Fig. 5(b). From this map, we extract the maximum negative frequency shift $\Delta\tilde{\omega}_{i,j}$ induced in the probed mode i due to the excitations in mode j. This protocol is repeated for increasing pump powers to extract the dependence of $\Delta\tilde{\omega}_{i,j}$ on pump power [see Fig. 5(c)]. The extraction of the cross-Kerr coefficient, defined as the frequency shift per excitation in the pumped mode, requires calibration of the input line attenuation to convert the applied pump power to the average excitation number in the mode. We perform this calibration using a separate device [66] connected via a microwave switch to the same measurement lines, following the procedure described in Sec. C 3. We repeat the full protocol across different bare SQUID array resonator frequencies to obtain the data markers shown in Figs. 5(d) and 5(e). The cross-Kerr measurement protocol is further detailed in Sec. D 7 of the Appendix.

We measure seven distinct cross-Kerr shifts as a function of ω_{SQ}, as shown in Fig. 5(e). The maximum cross-Kerr values of the probed modes range from 14 to 88 kHz.

Notably, we observe nonzero cross-Kerr interactions for multiple SAW modes simultaneously (i.e., for a given bare SQUID array resonator frequency), which provides further evidence that the system operates in the multimode coupling regime. To quantitatively analyze the data, we perform a global fit of all cross-Kerr measurements using Eq. (6b). The SQUID array resonator participation ratios are known from prior mode hybridization analysis (Fig. 3), and they are shown as dashed lines in Fig. 5(e). This leaves the bare SQUID Kerr nonlinearity χ_{SQ} as the only free parameter. The fit yields $\chi_{SQ}/2\pi = 0.57^{+0.15}_{-0.12}$ MHz, and the resulting curves (solid lines) show excellent agreement with the experimental data.

Additional self-Kerr measurements are provided in the Appendix in Fig. 22.

III. DISCUSSION AND CONCLUSION

In this work, we have explored a nonlinear multimode mechanical system realized by coupling multiple confined SAW modes to a nonlinear, flux-tunable SQUID array resonator. We demonstrate that the device operates at the onset of the mechanical multimode (or superstrong) coupling regime. By measuring the participation ratio of the SQUID array resonator in the hybridized modes, we show that both the induced mechanical nonlinearity and the total mode dissipation are accurately captured by this single metric. The ability to probe SAW and SQUID array resonator modes independently allows us to validate this model through direct measurements of both mode-dependent dissipation and cross-Kerr interactions between mechanical modes.

A key signature of the multimode coupling regime is that the SQUID array resonator participation ratio, $|u_{SQ,i}|^2$, remains well below 50% even at maximum hybridization with the mechanical modes. In our device, in particular, we measure a maximum participation ratio as low as 4%. While this behavior was previously modeled in Ref. [45], it had not been directly measured. Here, we introduce a simple and general method to extract participation ratios from the derivatives of the hybrid mode frequencies with respect to the bare SQUID array resonator frequency. This approach is particularly relevant because participation-ratio-based modeling is a standard design tool in superconducting quantum circuits [63], yet experimental extraction is often challenging. Our method is broadly applicable, including to complex systems where numerical modeling is impractical.

Another distinctive feature of the multimode coupling regime is the simultaneous inheritance of nonlinearity by several mechanical modes. This is confirmed through two-tone cross-Kerr measurements, which reveal sizeable phonon-phonon interactions mediated by the nonlinear ancilla.

1. Steady-state dynamics with two-photon drive

Weakly nonlinear electromagnetic modes have already enabled a broad range of applications in quantum science, including parametric amplification [67,68], frequency conversion [69], quantum sensing [55,70,71], quantum simulation of Ising-like networks [72,73], nonreciprocal coupling schemes [74,75], and signature of quantum chaos [66]. Our work extends these paradigms to the mechanical domain by using a platform that offers direct control and readout of acoustic modes via a dedicated IDT, which combined with the flux line of the SQUID array allows the study of various parametric phenomena with multiple acoustic modes. For example, applying a parametric drive at the frequency difference between SAW modes should enable the parametric coupling of acoustic modes [32], with the possibility of combining multiple parametric drives to realize synthetic topological phononic lattices [75–77]. In addition, the possibility of applying two-photon drives to the flux line of the nonlinear electromagnetic mode can produce first- and second-order dissipative phase transitions with correlated quantum fluctuations in the critical region [53], which may be inherited by the mechanical modes.

We explore this direction in Fig. 6 where we report the mechanical output field measured at port 3 at frequency ω_p while applying a two-photon drive at $2\omega_p$ through the flux line (see Fig. 1). In this configuration, the bare SQUID array frequency is set to $\omega_{SQ}/2\pi = 3.965$ GHz, detuned enough such that the detected signal corresponds predominantly to a single mechanical mode. The output field is demodulated at ω_p and integrated over time to obtain the population, while the corresponding quadratures histograms are shown in the lower panels.

By sweeping ω_p near a mechanical mode, five distinct dynamical regimes emerge. For large drive frequency, the output remains vacuum-like (pentagon marker). As the frequency is reduced, two metastable coherent states appear with opposite phase (triangle marker), which increase in amplitude upon further lowering the frequency (diamond marker). At a specific frequency (square marker), we observe a trimodal distribution. The corresponding time trace shown in Fig. 6(b) displays switching between the vacuum state and the two coherent states, indicating a first-order dissipative phase transition. Finally, once the drive frequency is below the critical region, the system stabilizes back into the vacuum-like configuration (circle marker).

Importantly, this response is not limited to a single mechanical resonance. We observe qualitatively similar two-photon–induced nonlinear switching across several hybridized modes. The downconverted signal at ω_p is also measured from the coupler IDT port 2. Complete information on the measurement protocol are added in Appendix D 8. While a complete analysis of multimode

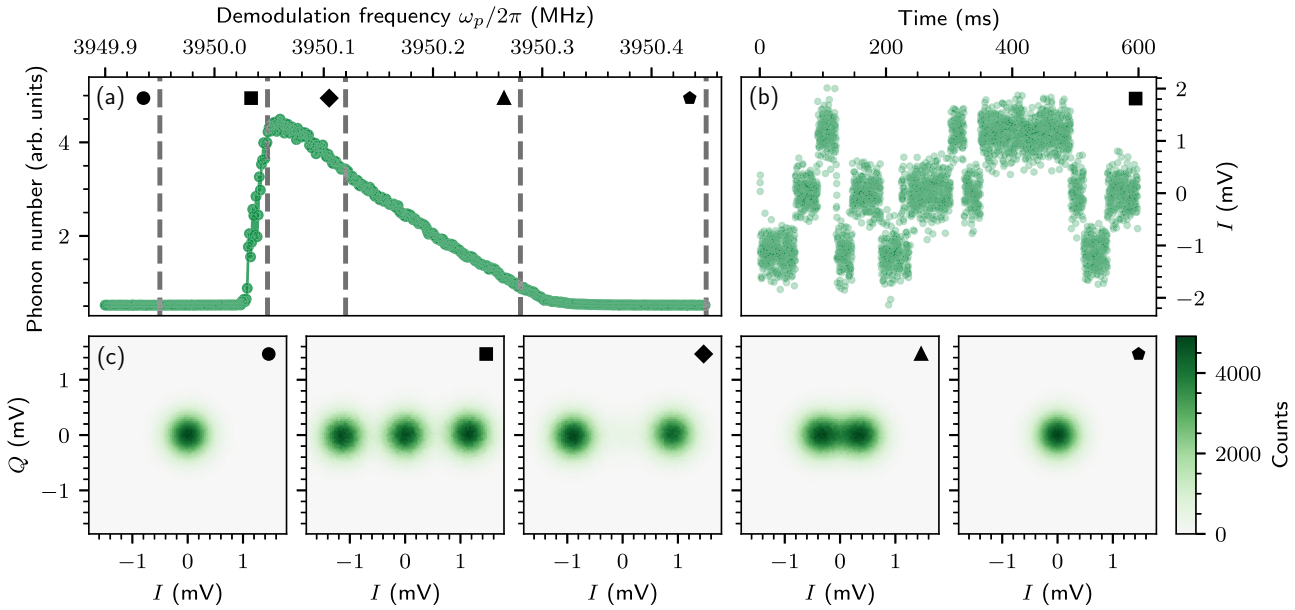


FIG. 6. Two-photon drive response of a mechanical mode. (a) Average phonon emission collected from surface acoustic wave port 3 while applying a two-photon drive to the SQUID array flux line at frequency $2\omega_p$ and demodulating the output at ω_p. The SQUID array is detuned in this configuration, and the detected field predominantly corresponds to mechanical excitation. (b) Representative time trace of the demodulated emission field in the vicinity of the nonlinear response region. The system intermittently switches between the vacuum state and two coherent states of opposite phase, consistent with a first-order dissipative transition. For clarity, only one in every ten data points is shown. (c) Quadrature histograms of the emission field at selected frequencies. Far from resonance, the distribution is vacuum-like. Near resonance, two well-separated coherent states emerge, which subsequently coexist with the vacuum state in the bistable region before collapsing back to vacuum once the drive is tuned beyond the nonlinear threshold. Markers correspond to different drive frequencies.

criticality lies beyond the scope of this work, the ability to induce and monitor two-photon parametric effects across multiple acoustic modes suggests a promising route toward study of multimode phase transitions [78] and enhanced critical sensing [56,79].

2. Toward multiple mechanical qubits

On the other hand, strongly nonlinear electromagnetic modes have enabled the realization of a single mechanical qubit using a bulk acoustic resonator coupled to a transmon qubit [29]. In the following, we explore the feasibility of extending our current platform to enable multiple mechanical qubits by replacing the weakly nonlinear SQUID array resonator with a single SQUID of reduced Josephson energy E_J. This yields a transmon qubit with excitation frequency around 4 GHz and anharmonicity $-2\chi_{tr} \approx E_C/\hbar \approx 2\pi \cdot 200\,\mathrm{MHz}$. Notably, the capacitance of the SQUID array resonator's IDT in our current design—approximately 70 fF—is already within the typical range for transmon qubits.

However, replacing the weakly nonlinear SQUID array resonator with a transmon pushes the system into a strongly nonlinear regime where our previously used participation-ratio-based analysis becomes inapplicable. This approach treats the nonlinearity as a perturbation [47,62,63], which breaks down when $|\chi_{tr}| \gtrsim g$ [80]. Indeed, while Eq. (6b) predicts that the hybrid modes self- and cross-Kerr always retain the sign of the bare nonlinearity, this no longer holds in the strongly nonlinear case, where a straddling regime may emerge, inducing sign changes in the nonlinearities [81,82].

To address these challenges, we model the transmon and each SAW mode as three-level systems and employ exact numerical diagonalization to compute the low-energy excitation spectrum. This enables us to identify parameter regimes where multiple mechanical modes acquire sufficient anharmonicity and retain enough coherence to function as qubits.

For simplicity, we simulate five SAW modes with uniform FSR $\Delta\omega$ and equal coupling g. We consider two coupling scenarios (illustrated in Fig. 7): (i) a weak-coupling regime where the SAW-transmon coupling g is much smaller than the free spectral range $\Delta\omega$ of the SAW cavity, $g = \Delta\omega/6$ (left column), and (ii) a multimode coupling regime where $g = \Delta\omega/2$ (right column).

In the single-mode coupling case, only one mechanical mode strongly hybridizes with the transmon at a time, resulting in well-separated anharmonicity peaks for each hybrid mode, with a maximum value of $2\tilde{\chi} = \pm g(2 - \sqrt{2})$ [29] [Fig. 7(c)]. The hybrid mode decoherence rate is estimated as $\Gamma_2 = \tilde{\kappa}/2$, using Eq. (5) and assuming a

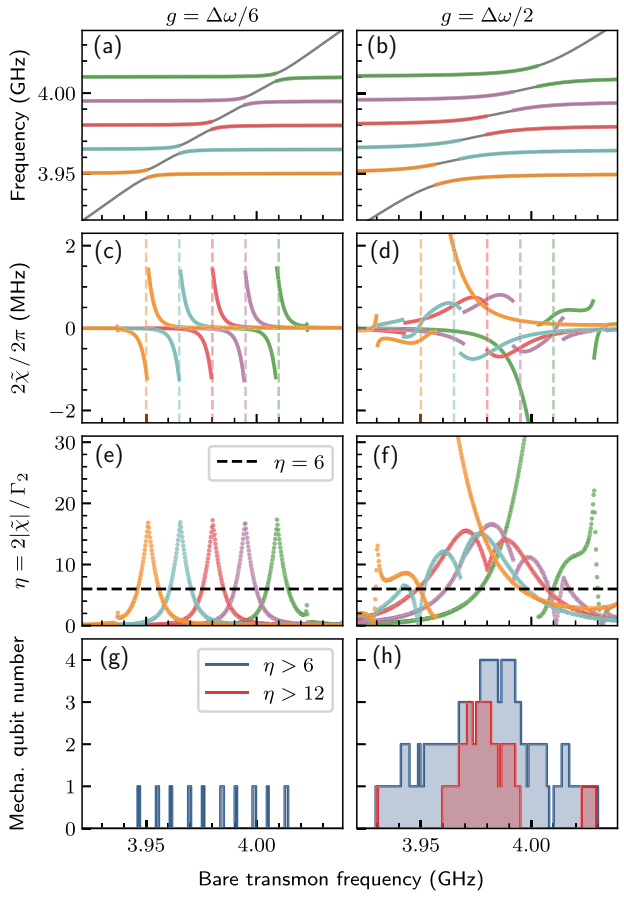


FIG. 7. Multiple mechanical qubits. Numerical simulation of a multimode system analogous to the device presented in the work, with the SQUID array resonator replaced by a transmon qubit of self-Kerr $\chi_{tr}/2\pi = -E_C/2h = -100$ MHz. For simplicity, we consider only five surface acoustic wave modes with uniform free spectral range $\Delta\omega/2\pi = 15$ MHz. Two coupling regimes are depicted: constant surface acoustic wave-transmon coupling $g = \Delta\omega/6$ (left column) and $g = \Delta\omega/2$ (right column). (a) and (b) Fundamental transitions frequencies $\tilde{\omega}_{g,e}/2\pi$. For each bare transmon frequency, we identify the hybrid mode in which a given bare surface acoustic wave mode has maximum participation and color it according to the corresponding bare surface acoustic wave mode. (c) and (d) Anharmonicity of the hybrid modes. The spectrum is computed by exact numerical diagonalization within the two-excitation manifold. For each fundamental transition $\tilde{\omega}_{g,e}$, all corresponding transitions $\tilde{\omega}_{e,f}$ and their anharmonicities $2\tilde{\chi} = \tilde{\omega}_{e,f} - \tilde{\omega}_{g,e}$ are computed. Only the smallest absolute anharmonicity per mode is shown; the full spectrum is presented in the Appendix. Bare surface acoustic wave mode frequencies are indicated by vertical dashed lines. (e) and (f) Ratio of anharmonicity to decoherence rate $\eta = 2|\tilde{\chi}|/\Gamma_2$. We assume dissipation rates for bare surface acoustic wave modes ($\kappa/2\pi = \Gamma_2/\pi = 50$ kHz) and for the transmon $\kappa_{tr}/2\pi = \Gamma_2/\pi = 300$ kHz [16]. Hybrid mode dissipation rates are calculated via Eq. (5). A hybrid mode is designated as a qubit if $\eta > 6$ (above the black dashed line) [29]. (g) and (h) Number of mechanical qubits as a function of bare transmon frequency, with transmon participation ratio $|u_{tr}|^2$ below 20%. Blue indicates $\eta > 6$, while red indicates $\eta > 12$.

typical transmon dissipation rate $\kappa_{tr}/2\pi = 300$ kHz [16] [Fig. 7(e)].

We define a hybrid mode to be qubit-like if its anharmonicity-to-decoherence ratio $\eta = 2\tilde{\chi}/\Gamma_2$ exceeds 6 [29], and further restrict to predominantly mechanical modes by requiring transmon participation $|u_{tr}|^2 < 20\%$. In this regime, only one such mechanical qubit can be realized at a time [Fig. 7(g)].

In contrast, in the multimode coupling case, all SAW modes hybridize simultaneously with the transmon, leading to a more complex anharmonicity structure [Fig. 7(d)]. Although the coupling increases, the maximum achievable anharmonicity remains comparable to the weak-coupling case. Crucially, however, all modes acquire significant anharmonicity. Accounting for hybrid mode dissipation, we find that placing the transmon frequency at the center of the SAW cavity bandwidth enables all five SAW modes to cross the qubit threshold [Fig. 7(f)]. Up to four of these modes satisfy the condition $|u_{tr}|^2 < 20\%$, thus qualifying as predominantly mechanical qubits [Fig. 7(h)].

Upgrading our current platform to realize multiple mechanical qubits is within realistic experimental reach. The required increase in FSR and coupling—approximately a factor of two—can be achieved by halving the effective SAW cavity length. In addition, although we simulated only five modes with $\Delta\omega = 15$ MHz, more than ten longitudinal SAW modes can be confined within the bandwidth used in this work.

In our current design, the dissipation of the SQUID array resonator is dominated by coupling to the readout feedline (see Fig. 18). This can be mitigated by reducing the coupling capacitance. Moreover, with improved fabrication techniques—such as surface cleaning prior to qubit deposition [83]—the internal loss rate of the transmon could be reduced down to $\kappa_{tr}/2\pi = 300$ kHz [16], as assumed in our simulations. Finally, qubit dissipation may be decreased even further by employing flip-chip architectures [15], which further suppress dielectric and radiation losses Fig. 11.

Altogether, leveraging the multimode coupling regime in SAW-based systems offers a compelling route toward realizing acoustic qubits with always-on self- and cross-Kerr interactions and long-range connectivity. It is important to notice that in the presented simulation, the anharmonicity of the mechanical qubits never exceeds one order of magnitude of the dissipation. Therefore, while in this architecture preparation fidelity of nonclassical mechanical state is going to be limited, this platform is particularly attractive for quantum simulation of quantum fluids of sound [84].

Mechanical qubits confined to the surface provide further advantages over bulk implementations, including improved accessibility, the ability to support multiple coupling points [4], and tighter confinement of acoustic mode

volumes. These features enhance prospects for strong coupling to elusive systems, such as charge or spin degrees of freedom [42], and enable integration with phononic waveguides for scaling [85].

ACKNOWLEDGMENTS

We thank Orjan Ameye, Santiago Salazar Jaramillo, Oded Zilberberg, Gustav Andersson, Guillaume Beaulieu and Filippo Ferrari for stimulating discussion regarding this work. M.S. acknowledges support from the EPFL Center for Quantum Science and Engineering postdoctoral fellowship. P.S. acknowledges the support by the Swiss State Secretariat for Education, Research and Innovation (SERI) under Contract No. UeM019-16 and also under Contract No. MB22.00081. P.S. also acknowledges the support of the Swiss National Science Foundation (SNSF), Grants No. 200021_200418/1 and No. 206021_205335. This work was supported by the Knut and Alice Wallenberg foundation through the Wallenberg Center for Quantum Technology (WACQT), and the Swedish Research Council, VR. The device was fabricated at MyFab Chalmers.

M.S., L.P., P.D. and P.S. designed the experiment. M.S. designed and fabricated the devices. M.S., C.B. and V.J. performed preliminary device measurements. L.P. and R.M.M. performed the measurements presented in the manuscript. L.P., R.M.M. and M.S. analyzed the data. L.P. and R.M.M. developed the theoretical models. P.S. and P.D. supervised the project. L.P., M.S., R.M.M. and P.S. wrote the manuscript with input from all authors.

DATA AVAILABILITY

The data that support the findings of this article are openly available [86].

APPENDIX A: SYSTEM PARAMETERS AND VARIABLES

In Table I the symbols employed in this work are summarized. In addition, Table II reports the geometric and cooldown (CD)-independent parameters of the device, while Table III shows the parameters extracted in the characterization of the device and of the measurement setup throughout several cooldowns. Finally, in Table IV each figure is matched with the cool downs when the data displayed were acquired.

TABLE I. Table of symbols.

Symbol	Description	Unit
ϕ_X	Magnetic flux threading SQUID array loops	Wb
$\omega_{SQ}/2\pi$	Bare SQUID frequency	Hz
$a; a^\dagger$	SQUID array resonator annihilation and creation operators	
$\kappa_{SQ}/2\pi$	Total dissipation rate of the bare SQUID array resonator	Hz
$\kappa_{SQ,ext}/2\pi$	External dissipation rate of the bare SQUID array resonator	Hz
$\kappa_{SQ,int}/2\pi$	Internal dissipation rate of the bare SQUID array resonator	Hz
$\chi_{SQ}/2\pi$	SQUID array resonator self-Kerr	Hz
$\omega_i/2\pi$	Bare SAW frequencies	Hz
$\Delta\omega_i/2\pi$	Free spectral range of bare SAW modes	Hz
$b_i; b_i^\dagger$	SAW mode annihilation and creation operators	
$\kappa/2\pi$	SAW mode total dissipation rate	Hz
$\kappa_{ext}/2\pi$	SAW mode external dissipation rate	Hz
$\kappa_{int}/2\pi$	SAW mode internal dissipation rate	Hz
$g_i/2\pi$	Coupling strength between the electromagnetic and mechanical modes	Hz
$\lvert u_{SQ,j}\rvert^2$	Participation of SQUID array resonator in the j th hybrid modes	
$\lvert u_{i,j}\rvert^2$	Participation of ith SAW mode in j th hybrid mode	
$\tilde{\omega}_i/2\pi$	Frequency of hybrid modes	Hz
$c_i; c_i^\dagger$	Hybrid mode annihilation and creation operators	
$\tilde{\kappa}_j/2\pi$	Total dissipation rate of the hybrid modes	Hz
$\tilde{\chi}_{ij}/2\pi$	Kerr coefficients among the hybrid modes	Hz
$\Delta\tilde{\omega}_{i,j}/2\pi$	Maximum displacement of ith hybrid mode when pumping the j th hybrid mode	Hz
$\kappa_{tr}/2\pi$	Total dissipation of transmon qubit	Hz
$\lvert u_{tr}\rvert^2$	Participation of trasmon qubit in the hybrid modes	
$\chi_{tr}/2\pi$	Transmon qubit self-Kerr	Hz
$\eta = 2\tilde{\chi}/\Gamma_2$	Anharmonicity to decoherence ratio	
S_{21}	Normalized transmission notch-type coefficient measured from the SQUID array resonator feedline	
S_{33}	Normalized reflection coefficient measured from launcher IDT feedline	

TABLE II. Table of geometric and cooldown-independent parameters.

Parameter	Description	Value	Unit
λ_0	Wavelength of the central SAW mode	720	nm
$\omega_0^c/2\pi$	Central frequency of the SAW cavity	3.967(9)	GHz
r	Single finger reflectivity	3.9 %	
$\Delta_m/2\pi$	Bragg mirror bandwidth	99	MHz
d	Distance between Bragg mirrors	155.4	μm
L_c	Effective cavity length	165	μm
N_m	Number of fingers in each Bragg mirror	500	
N_p^{launcher}	Number of pairs of split fingers in launcher IDT	30	
N_p^{coupler}	Number of pairs of split fingers in coupler IDT	14	
N_s	Number of SQUIDs in the array	12	
K^2	Effective electromechanical coupling in GaAs	0.07 %	
W	Width of the launcher IDT	25	μm

APPENDIX B: THEORY

1. Model

a. Hamiltonian, Bogoliubov, nonlinearity expansion

The Hamiltonian of a linear bosonic mode, a_0, coupled to n other uncoupled linear bosonic modes, $a_{i>0}$, can be written as

$$H_0/\hbar = \omega_{\text{SQ}} a_0^\dagger a_0 + \sum_{i>0}^{n} \omega_i a_i^\dagger a_i - (a_0 - a_0^\dagger) \sum_{i>0}^{n} g_i (a_i - a_i^\dagger), \tag{B1}$$

with the usual bosonic commutation relations $[a_k, a_l^\dagger] = \delta_{kl}$. To map the model to our device we can identify a_0 with operator of SQUID array resonator, and $a_{i>0}$ with the ones for the *ith* bare SAW mode. This Hamiltonian takes into account particle nonconserving terms such as $a_0 a_i$ and $a_0^\dagger a_i^\dagger$, so a priori the diagonalization should be performed via Bogoliubov transformation. This protocol is usually employed in many-body condensed matter physics to diagonalize quadratic Hamiltonians by combining the original creation and annihilation operators via a symplectic transformation Q, preserving the original bosonic algebra.

In the first place, the Hamiltonian Eq. (B1) can be rewritten as a quadratic form,

$$H_0/\hbar = \frac{1}{2} \begin{pmatrix} \boldsymbol{a}^\dagger & \boldsymbol{a} \end{pmatrix} \begin{pmatrix} T & U \\ U^* & T^* \end{pmatrix} \begin{pmatrix} \boldsymbol{a} \\ \boldsymbol{a}^\dagger \end{pmatrix} + \text{const.} \tag{B2}$$

Here "const." is a diagonal matrix with the vacuum energy of the different fields, and we define $\begin{pmatrix} \boldsymbol{a}^\dagger & \boldsymbol{a} \end{pmatrix} =$

TABLE III. Device and measurement setup parameters. The measurements in this work were performed over several cooldowns. This table reports the parameters of the device and the attenuation of the input feedlines employed in the different cooldowns. "/" denotes missing values for the specific cooldown. In the 20240927CD and subsequent cooldowns, we added 20dB attenuation at room temperature compared to the 20240913CD. Other changes and calibration methods are explained in Sec. C 3.

Parameter	Description	20240913CD	20240927CD	20241206CD	20250214CD	Unit
$\omega_{\text{SQ},0}/2\pi$	SQUID array resonator frequency at sweetspot	4.70 ± 0.04	4.709 ± 0.003	4.7095 ± 0.0002	/	GHz
α_{SQ}	Voltage-to-reduced-flux conversion factor	1.14 ± 0.04	1.083 ± 0.003	1.0852 ± 0.0008	/	rad/V
$V_{\text{SQ},0}$	Voltage offset at sweetspot	2.6 ± 3	35 ± 2	39.5 ± 0.2	/	mV
$\kappa_{\text{SQ}}/2\pi$	Bare SQUID dissipation inside Bragg bandwidth	8.8 ± 0.7	/	/	/	MHz
$\chi_{\text{SQ}}/2\pi$	Bare SQUID array resonator nonlinearity	/	/	$0.57^{+0.15}_{-0.12}$	/	MHz
A^{SQ}	Attenuation of the SQUID array resonator feedline (port 1)	-78.8 ± 2	-97 ± 1.5	-101 ± 1	-102 ± 1.5	dB
A^{IDT}	Attenuation of the launcher IDT feedline (port 3)	-78.8 ± 2	-97 ± 2	/	-103.6 ± 2	dB

TABLE IV. Association between measurement and cooldown.

Figure	Description	CD
Main text		
Fig. 2	Bare SAW modes	20240913CD
Fig. 3(a)	Flux sweep of the SQUID array resonator across SAW modes	20240927CD
Figs. 3(b) and 3(c)	Flux sweep of the SQUID array resonator across SAW modes	20240913CD
Fig. 4	Characterization of the multimode coupling regime	20240913CD
Fig. 5	Cross-Kerr measurement versus bare SQUID array resonator frequency	20241206CD
Fig. 6	Two-photon driven acoustic modes	20251031CD
Appendix		
Fig. 13	Input line attenuation calibration	20241206CD
Fig. 14	Frequency and dissipation rates of bare SAW modes	20240913CD
Fig. 15	Frequency difference between SAW modes	20240913CD
Fig. 17	Internal dissipation rate of SAW modes as a function of input power	20250214CD
Fig. 18	Dissipation of SQUID Array versus Flux	20240927CD
Fig. 20	Additional data for Fig. 4	20240913CD
Fig. 21	Mode participation and dissipation rate analysis in presence of a spurious SAW mode	20240913CD
Fig. 22	Self-Kerr measurement at one flux value	20241206CD
Fig. 23	Cross-Kerr measurement at one flux value	20241206CD

$\left(a_0^\dagger, a_1^\dagger, \ldots, a_n^\dagger,\ a_0, a_1, \ldots, a_n\right)$, the hermitian adjoint of this vector as $\binom{\boldsymbol{a}}{\boldsymbol{a}^\dagger} = \left(\boldsymbol{a}^\dagger\ \boldsymbol{a}\right)^\dagger$, and the matrices T and U in the basis $\mathcal{B}_a = \{a_0, a_1, \ldots, a_n\}$ can be written as

$$T_{\mathcal{B}_a} = \begin{pmatrix} \omega_{\mathrm{SQ}} & g_1 & \cdots & g_n \\ g_1 & \omega_1 & \cdots & 0 \\ \vdots & \vdots & \ddots & \vdots \\ g_n & 0 & \cdots & \omega_n \end{pmatrix} \tag{B3}$$

$$\text{and } U_{\mathcal{B}_a} = \begin{pmatrix} 0 & -g_1 & \cdots & -g_n \\ -g_1 & 0 & \cdots & 0 \\ \vdots & \vdots & \ddots & \vdots \\ -g_n & 0 & \cdots & 0 \end{pmatrix}. \tag{B4}$$

Following the protocol introduced in Ref. [61], we write the commutator of the a-bosons in a matrix form and obtain the metric Ω, which guarantees that the transformation Q preserves the commutation relations

$$[X, X^\dagger] \equiv XX^\dagger - (X^\dagger)^T X^T = \Omega, \tag{B5}$$

$$\Omega = \begin{bmatrix} \mathbb{I}_{n+1} & 0 \\ 0 & -\mathbb{I}_{n+1} \end{bmatrix}, \tag{B6}$$

where $X \equiv \left(\boldsymbol{a}^\dagger\ \boldsymbol{a}\right)$, for compactness of the notation. Therefore, the orthonormalization condition for the transformation Q, (also referred to as symplectic condition) reads as

$$Q, \Omega \in \mathbb{M}_{2(n+1)\times 2(n+1)}(\mathbb{C}) \quad : \quad Q\Omega Q^\dagger = \Omega. \tag{B7}$$

This condition can be recast into the following relation on the inverse of the transformation:

$$Q^{-1} = \Omega^{-1} Q^\dagger \Omega \iff Q^\dagger = \Omega^{-1} Q^{-1} \Omega. \tag{B8}$$

Leveraging Eq. (B8), the diagonalization of the hamiltonian matrix H can be rewritten as

$$\begin{aligned} Q^\dagger \mathrm{H} Q = D \rightarrow\ & (\Omega^{-1} Q^{-1} \Omega)\mathrm{H} Q = D \\ \rightarrow\ & Q^{-1}(\Omega\mathrm{H}) Q = \Omega D, \end{aligned} \tag{B9}$$

where D is the diagonal matrix with the eigenvalues of ΩH. In the most general context Q can be obtained from $Q_{\Omega\mathrm{H}}$, the transformation diagonalizing ΩH, by means of subsequent rotations within the eigenspaces associated to each distinct eigenvalue. However, thanks to the symmetries of the model, ΩH is **not singular and its spectrum is not degenerate**. Therefore, Q coincides with $Q_{\Omega\mathrm{H}}$, provided that the column eigenvectors of ΩH are orthonormalized (w.r.t. the conventional metric, $\mathbb{I}_{2(n+1)\times 2(n+1)}$). In addition, the structure of Q can be further constrained in the block form

$$Q = \begin{pmatrix} u & v \\ v^* & u^* \end{pmatrix} \text{ with } u, v \in M_{n\times n}(\mathbb{C}), \tag{B10}$$

and by restricting the coefficients to be real, the transformation connecting the **a** and the **c** bosons reads as

$$\begin{pmatrix} \boldsymbol{a} \\ \boldsymbol{a}^\dagger \end{pmatrix} = \begin{pmatrix} u & v \\ -v & u \end{pmatrix} \begin{pmatrix} \boldsymbol{c} \\ \boldsymbol{c}^\dagger \end{pmatrix} \text{ with } u, v \in M_{n\times n}(\mathbb{R}), \tag{B11}$$

where $\left(\boldsymbol{c}\ \boldsymbol{c}^\dagger\right) = \left(c_0, c_1, \ldots, c_n, c_0^\dagger, c_1^\dagger, \ldots, c_n^\dagger\right)$.

b. Kerr term

Now we take into account that the common mode a_0 is, in fact, nonlinear. Namely, we perturbatively transform the self-Kerr term $\chi_{\mathrm{SQ}}/6\left(a_0 + a_0^\dagger\right)^4$ according to Eq. (B11).

By selecting the terms of the form $(c_i^\dagger c_i)^2$ and $c_i^\dagger c_i c_j^\dagger c_j$, we find an expression for the self- and cross-Kerr of the $\boldsymbol{c}$-bosons on participation of a_0 and $a_0^\dagger$ in the hybrid modes,

$$\frac{\chi_{\mathrm{SQ}}}{6}(a_0+a_0^\dagger)^4 \to \tilde{\chi}_{ii}(c_i^\dagger c_i)^2 + \tilde{\chi}_{ij}(c_i^\dagger c_i c_j^\dagger c_j) + \ldots, \tag{B12a}$$

$$\tilde{\chi}_{ii} = \chi_{\mathrm{SQ}}(u_{0,i}-v_{0,i})^4, \tag{B12b}$$

$$\tilde{\chi}_{ij} = 2\chi_{\mathrm{SQ}}(u_{0,i}-v_{0,i})^2(u_{0,j}-v_{0,j})^2, \tag{B12c}$$

where $\tilde{\chi}_{ii}$ and $\tilde{\chi}_{ij}$ are the self- and the cross-Kerr respectively. The cross-Kerr term complies with the relation provided in Ref. [62].

c. Simplified model

Following the scheme introduced above to numerically diagonalize the Hamiltonian matrix H, for the coupling regime of our device, we find that the coefficients of the v matrix can be neglected with respect to the ones of the u matrix. In fact, the model (B1) reduces to a particle conserving Hamiltonian, equivalent to performing rotating-wave approximation,

$$H_0/\hbar \approx \omega_{\mathrm{SQ}} a_0^\dagger a_0 + \sum_{i>0}^{n} \omega_i a_i^\dagger a_i + \sum_{i>0}^{n} g_i(a_0^\dagger a_i + a_i^\dagger a_0), \tag{B13}$$

which in matrix form simplifies to

$$H/\hbar \approx \boldsymbol{a}^\dagger T_{\mathcal{B}_a} \boldsymbol{a} + \mathrm{const}, \tag{B14}$$

with the same meaning of the symbols as above. Thus, the Hamiltonian Eq. (B14) is diagonalized just by the u transformation. This model is equivalent to Eq. (1) after identifying $a_0 \equiv a$, and $a_i \equiv b_i$ for $i > 0$. Finally, self- and cross-Kerr relations can be simplified as

$$\tilde{\chi}_{ii} \approx \chi_{SQ}\,(|u_{0,i}|^2)^2, \tag{B15a}$$

$$\tilde{\chi}_{ij} \approx 2\,\chi_{SQ}\,|u_{0,i}|^2\,|u_{0,j}|^2. \tag{B15b}$$

d. Participation from derivative

The participation of the SQUID resonator in the hybrid modes can be extracted from the derivative of the corresponding eigenenergy with respect to the bare SQUID frequency ω_{SQ}. First, we restrict to the single-excitation subspace, and consider eigenstates $|\tilde{\psi}_i\rangle$ with eigenenergies $\tilde{\omega}_i$. Then, by leveraging the Hellmann-Feynman theorem [87] and the fact that the projector onto a space of finite size is a bounded operator, thus continuous, we can write as follows:

$$\begin{aligned}\frac{\mathrm{d}\tilde{\omega}_i}{\mathrm{d}\omega_{\mathrm{SQ}}} &= \frac{\mathrm{d}}{\mathrm{d}\omega_{\mathrm{SQ}}}\langle\tilde{\psi}_i|H_0/\hbar|\tilde{\psi}_i\rangle = \langle\tilde{\psi}_i|\frac{\mathrm{d}H_0/\hbar}{\mathrm{d}\omega_{\mathrm{SQ}}}|\tilde{\psi}_i\rangle \\ &= \langle\tilde{\psi}_i|n_0|\tilde{\psi}_i\rangle = u_{0,i}^* u_{0,i},\end{aligned} \tag{B16}$$

where n_0 is the number operator of mode a_0, associated to the SQUID array resonator.

e. SQUID array resonator characteristics

$$\begin{aligned}\omega_{\mathrm{SQ}}(\phi_X)/2\pi &= \omega_{\mathrm{SQ},0}\sqrt{|\cos(\pi(\phi_X-\phi_0)/\Phi_0)|}/2\pi \\ &= \omega_{\mathrm{SQ},0}\sqrt{|\cos(\alpha(V-V_0))|}/2\pi,\end{aligned} \tag{B17}$$

where $\omega_{\mathrm{SQ},0}$ is the maximum frequency of the SQUID array resonator at zero flux, ϕ_X is the magnetic flux threading the SQUID loops, ϕ_0 the residual flux offset, and Φ_0 the magnetic flux quantum. Experimentally, the magnetic flux bias is applied by delivering a DC voltage across a $\approx 1\,\mathrm{k}\Omega$ bias resistor in series with an external superconducting coil located beneath the sample. As a result, the relevant calibration parameters for the SQUID array resonator are the conversion factor from voltage to reduced flux, α, and the voltage offset corresponding to the zero-flux point, V_0.

f. Input-output relations

The input-output relation employed to characterize the transmission signal in notch configuration, S_{21}, measured through port 1 and 2, is [88]

$$\underset{\omega_r,\phi,\kappa_{\mathrm{tot}},\kappa_{\mathrm{c}}}{S_{21}(\omega)} = 1 - \frac{\kappa_{\mathrm{c}}}{(\kappa_{\mathrm{tot}}+2i(\omega-\omega_{\mathrm{r}}))} \times \frac{e^{i\phi}}{\cos(\phi)}, \tag{B18}$$

where ω is the frequency of the probe tone, ω_{r} is the frequency of the mode, κ_{tot} is the total dissipation of the mode, κ_{c} is the external dissipation rate of the mode to the microwave line connecting ports 1 and 2. Finally, the extra parameter ϕ is used to account for small impedance mismatch in the readout lines [88,89].

The input-output relation employed to characterize the reflection signal measured from port 3 is

$$\underset{\omega_r,\phi,\kappa_{\mathrm{tot}},\kappa_{\mathrm{c}}}{S_{33}(\omega)} = 1 - \frac{2\,\kappa_{\mathrm{c}}}{(\kappa_{\mathrm{tot}}+2i(\omega-\omega_{\mathrm{r}}))} \times \frac{e^{i\phi}}{\cos(\phi)}, \tag{B19}$$

where here κ_{c} is the coupling rate of the mode to the feed line connected to port 3.

g. Conversion to excitation number

The relation to convert the input power into the steady-state average photon/phonon population of a linearly driven resonator is

$$\bar{n} = \frac{1}{\hbar\omega_r}\frac{\kappa_c}{\Delta^2 + (\kappa_{tot}/2)^2} \times P_{in,W} \times 10^{-|A|/10}, \quad \text{(B20)}$$

where $\Delta = \omega - \omega_r$ is the detuning of the probe tone, ω, from the resonator frequency ω_r, $P_{in,W}$ the power of the probe tone at room temperature in Watt, and A is the total attenuation of the line in dB as calibrated with the protocol described below in section Sec. C 3.

2. Outlook: Mechanical qubits

a. From weakly nonlinear modes to mechanical qubits

We have demonstrated that our platform offers control on acoustic mode nonlinearities by controlling the SQUID array resonator frequency. The effective nonlinearity of the hybridized modes is directly determined by the nonlinearity of the bare SQUID resonator and by the *square* of its participation ratio in each hybridized mode [Eq. (6a)]. To facilitate comparison with the literature on qubit systems [29,90], we define a dimensionless parameter of the quantum character of a mode as $\eta = 2|\chi|/\Gamma_2$, using its anharmonicity 2χ and decoherence rate $\Gamma_2 = \kappa/2$. In this work, the SQUID array resonator is only moderately nonlinear, with $\eta_{SQ} = 4|\chi_{SQ}|/\kappa_{SQ} \approx 0.27$. As a result, the hybridized modes do not reach the quantum regime ($\eta > 1$) and $\eta_i = 4|\tilde{\chi}_i|/\tilde{\kappa}_i$ is at most 0.12 (Fig. 8). Nevertheless, as noted in the main text, this moderate nonlinearity regime is attractive for applications such as parametric processes, frequency conversion and squeezing, and quantum sensing with multimode massive objects.

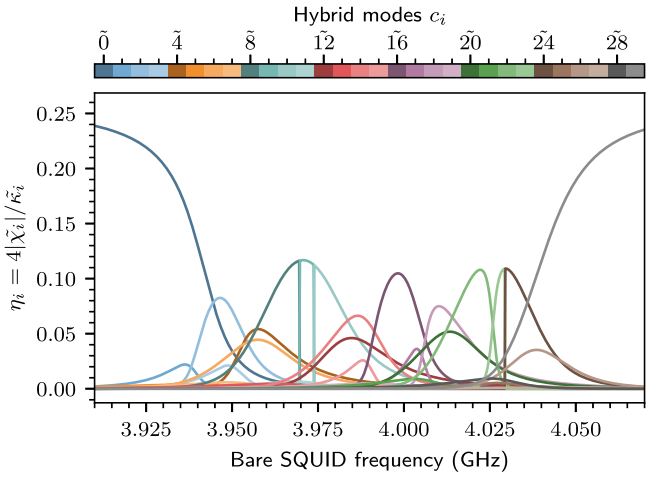


FIG. 8. Ratio between anharmonicity $2|\tilde{\chi}_i|$ and decoherence rate $\tilde{\kappa}_i/2$ for all hybrid modes of the SQUID array device presented in this work. We compute the anharmonicity to decoherence rate ratio $\eta = 4|\tilde{\chi}_i|/\tilde{\kappa}_i$ using Eqs. (5) and (6a). Different colors indicate the 30 hybrid modes c_i.

It was shown that coupling a low loss microwave cavity to a transmon qubit can lead to a cavity with inherited self-Kerr much larger than its dissipation [91]. This principle was recently extended to a bulk acoustic wave resonator [29] to realize a single mechanical qubit. We propose to use the architecture introduced in our work to extend this breakthrough to the multimode regime to realize a network of mechanical qubits.

b. Failure of participation-ratio analysis

As demonstrated in this work, the participation-ratio analysis provides quantitative agreement with measurements in the weak nonlinearity regime. However it is known that this method can fail for small detuning even for moderately anharmonic circuits like transmon qubits. To be more quantitive, let us consider a transmon qubit with angular frequency ω_q and anharmonicity $E_C/h = -2\chi_{tr}/2\pi = 200\,\text{MHz}$, coupled to a single bosonic mode, with angular frequency ω_q. The self- and cross-Kerr of the two hybridized modes strongly deviate from participation ratio predictions [Eq. (6a)] for detuning $0 < \Delta < E_C/\hbar$, with $\Delta = \omega_q - \omega_r$. This regime is known as the straddling regime [81,90], in which higher levels of the nonlinear resonator cause the self- and cross-Kerr to change sign and show more complicated behavior. In the limit of very large anharmonicity, $|\chi| \gg |\Delta|, g$, the nonlinear resonator can be approximated as a two-level system. We then retrieve the celebrated Jaynes Cummings model [90]. The nonlinearity of the two hybrid modes is then given by [29]

$$\tilde{\chi} = -\frac{1}{4}\Delta \pm \frac{1}{4}\left(2\sqrt{\Delta^2 + 4g^2} - \sqrt{\Delta^2 + 8g^2}\right). \quad \text{(B21)}$$

In this regime, the nonlinearity of the hybrid modes at $\Delta = 0$ is independent of the transmon anharmonicity and is instead limited by the coupling g. This is very different from the prediction of participation-ratio analysis [Eq. (6a)], where at resonance the participation ratio is 50 % and the self-Kerr of hybrid modes is $\tilde{\chi} = \chi_{tr}/4$, which is independent of g. The intermediate regime, where $|\chi| \simeq |\Delta|, g$, is more complicated but can be addressed using full numerical diagonalization.

c. Numerical diagonalization

To obtain anharmonicities of hybrid system for any resonator nonlinearity, e.g., in the straddling regime, we can resort to exact numerical diagonalization. We include three levels for all acoustic modes $\hat{a}_i$ and transmon qubit $\hat{b}$, and use qutip [92] to find the system eigenvalues and eigenvectors. In Fig. 7 we consider a simplified system of five acoustic modes, equally spaced in frequency with $\Delta\omega/2\pi = 15\,\text{MHz}$. The anharmonicity of the transmon

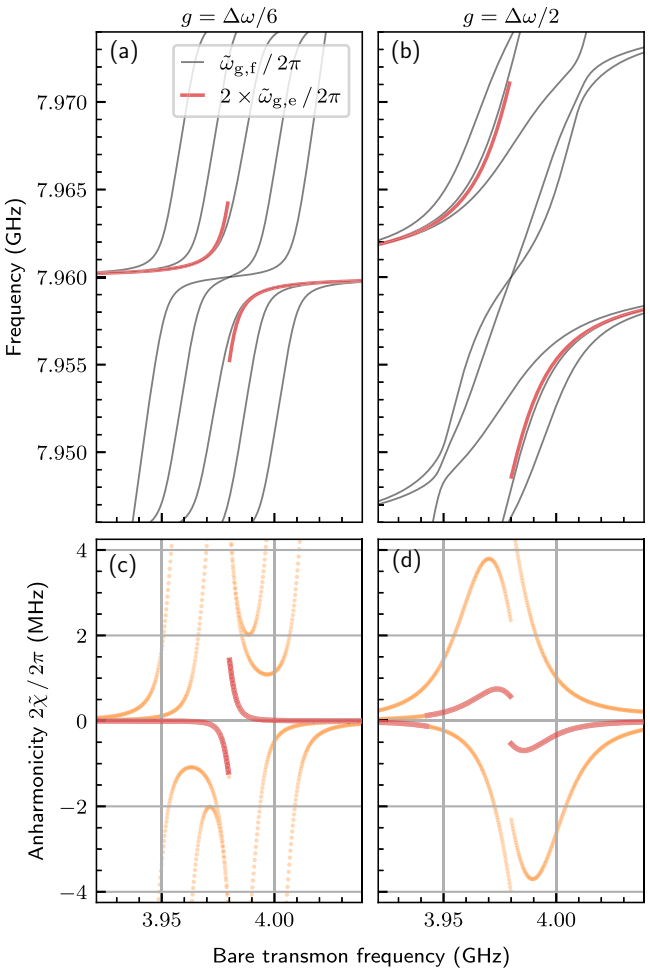


FIG. 9. Two-excitation subspace and anharmonicities. Simulations use the same model as in Fig. 7. (a) and (b) Part of the two-excitation energy levels $\tilde{\omega}_{g,f}/2\pi$ (gray lines) zoomed-in around twice the single ground state transition energy $2 \times \tilde{\omega}_{g,e}/2\pi$ of the central acoustic mode (red). (c) and (d) Anharmonicities $2\tilde{\chi}/2\pi$ associated to the red hybrid mode of Figs. 7(a) and 7(b) within ±4 GHz are shown with orange circle markers. The smallest (in absolute value) anharmonicity is shown with a thick red line and corresponds to the anharmonicity shown in Figs. 7(c) and 7(d).

qubit is $2\chi_{\rm tr}/2\pi = -E_C/h = -200\,$MHz, corresponding to a typical transmon qubit [90]. We consider a uniform coupling between transmon and acoustic modes, with a single-mode coupling regime $g = \Delta\omega/6 = 2\pi \times 2.5\,$MHz, and a multimode coupling regime $g = \Delta\omega/2 = 2\pi \times 7.5\,$MHz. The single-excitation energy levels $\omega_{g,e}$ are reported in Figs. 7(a) and 7(b). The two-excitation energy spectrum contains 21 levels, part of which is shown with gray solid lines in Figs. 9(a) and 9(b). The red line shows twice the single-excitation energy of the red hybrid mode of Figs. 7(a) and 7(b), which corresponds mainly to the central acoustic mode with bare frequency 3.98 GHz. To define the anharmonicity of this hybrid mode, we compute the frequency differences $2\tilde{\chi} = \tilde{\omega}_{e,f} - \tilde{\omega}_{g,e}$ for all two-excitation levels $\tilde{\omega}_{e,f}$, i.e., half the difference between the red line and all gray lines. We thus get several anharmonicities $2\tilde{\chi}$ (21 for 5 acoustic modes). The one within ±4 MHz are reported in Figs. 9(c) and 9(d) with orange markers. The smallest absolute anharmonicity per bare transmon frequency is shown with a thicker red line, and corresponds to the value shown in Figs. 7(c) and 7(d). Some of the transitions may have zero matrix elements, but we consider the most stringent case by including all transitions.

A hybrid mode can be considered a qubit if its smallest anharmonicity (by magnitude) is much larger than its decoherence rate. However, to be considered a *mechanical* qubit, it should have a weak bare qubit participation ratio $|u_{\rm tr}|^2$. To identify mechanical qubits in Fig. 7, we decompose the hybrid modes in the bare mode basis, as shown in Fig. 10. The bare qubit participation is shown with black dashed lines, and we only consider hybrid modes with participation weaker than $|u_{\rm tr}|^2 < 20\%$.

d. Effect of transmon qubit dissipation rate

In Fig. 7, we assumed a moderate total dissipation rate for the transmon qubit, $\kappa_{\rm tr}/2\pi = 300\,$kHz, which is consistent with values reported in the literature for direct fabrication of transmons on GaAs [16]. However, this value is lower than what we measured for the SQUID array resonator in this work, $\kappa^{\rm extra}_{\rm SQ,int}/2\pi = 2\,$MHz (Fig. 18). We numerically investigated the impact of the transmon qubit dissipation rate on the number of mechanical qubits, fixing all the others parameters as in Fig. 7. For $\kappa_{\rm tr}/2\pi = 600\,$kHz, we still obtain four mechanical qubits over an extended range of bare transmon frequencies. For $\kappa_{\rm tr}/2\pi = 1000\,$kHz, three mechanical qubits remain accessible. At $\kappa_{\rm tr}/2\pi = 1500\,$kHz, only a single mechanical qubit can be realized; however, it is possible to recover four simultaneous mechanical qubits by increasing both the coupling strength g and the FSR.

The dissipation rate of the transmon qubit can be further reduced by using a flip-chip integration technique [93–95], where all components except the transmon qubit are fabricated on GaAs, and the qubit is fabricated on a silicon or sapphire substrate. Such architectures have been experimentally demonstrated, yielding transmon qubit lifetimes of $\approx 10\,\mu$s [94]. In Fig. 11, we assume a compatible transmon decoherence rate of $\kappa_{\rm SQ}/2\pi = 2\Gamma_2/2\pi = 25\,$kHz. We also assume reduced SAW dissipation rates, setting $\kappa/2\pi = 25\,$kHz, which has been demonstrated on similar GaAs substrates with optimized IDT and Bragg mirror designs [28].

e. Optimizing the number of mechanical qubits

We note that increasing the coupling g excessively can be detrimental to the realization of multiple mechanical qubits. In fact, in this regime, the transmon participation

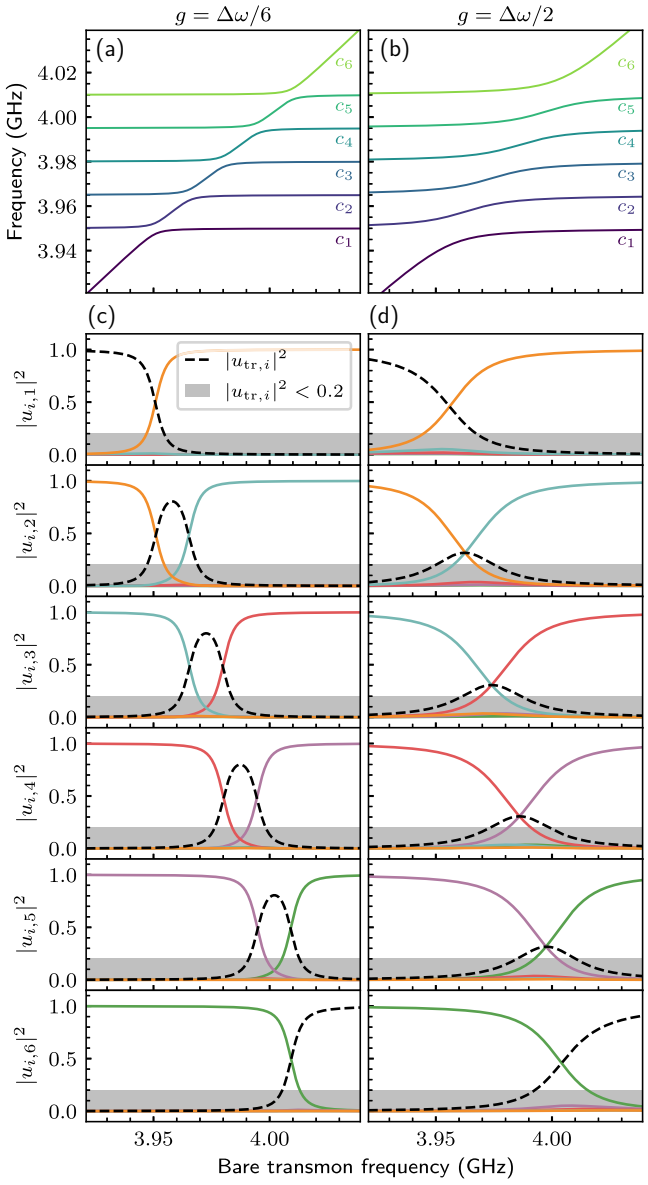


FIG. 10. Bare modes participation in hybrid qubits. Simulations use the same model as in Fig. 7. (a) and (b) The single-excitation energy spectrum is reproduced from Figs. 7(a) and 7(b). Each color corresponds to a different hybrid mode from c_1 to c_6. (c) and (d) Hybrid modes decomposition in the bare mode basis. Each row corresponds to the decomposition of one hybrid mode of (a) and (b). The bare transmon participation ratio is shown in black dashed lines, while the participation of other bare acoustic modes is shown with colored solid lines. The area shaded in gray corresponds to hybrid modes with transmon participation under 20 %, which we classify as mainly mechanical.

in the hybrid modes becomes vanishingly small, except for the first and last hybrid modes of the passband, which retain substantial transmon participation. This behavior is akin to the formation of atom-photon bound states in systems with dispersion relations featuring band gaps [96]. Therefore, the coupling g should be kept smaller than

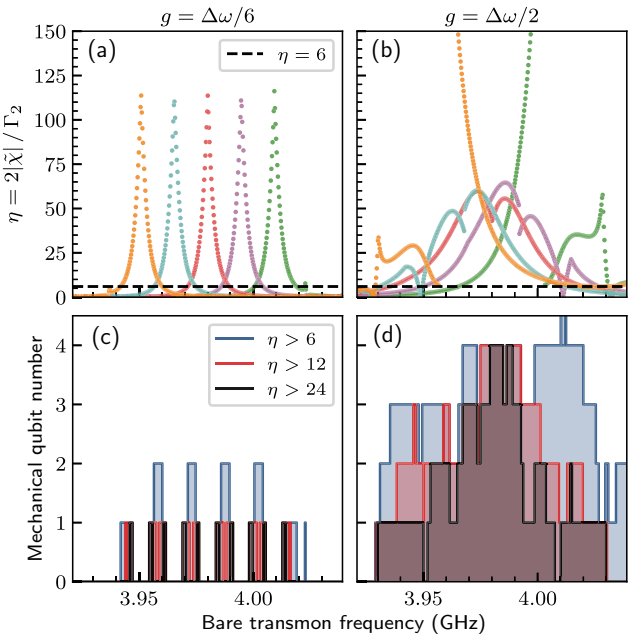


FIG. 11. Simulations for mechanical qubits with reduced dissipation rates. Simulations use the same model as in Figs. 7(e)–7(h), but with reduced total dissipation rates $\kappa_{\mathrm{SQ}}/2\pi = \kappa/2\pi = 25$ kHz, compatible with a flip-chip architecture. Compared to Fig. 7, the nonlinearity to decoherence ratios are larger [(a) and (b)], enabling mechanical qubits over a broader range of bare transmon frequencies and with larger nonlinearity to decoherence ratios [(c) and (d)].

the SAW cavity bandwidth to realize multiple mechanical qubits.

The transmon qubit anharmonicity can also be optimized to maximize the number of mechanical qubits. In the regime where $\chi_{\mathrm{tr}} \gg g$, the anharmonicity of the hybrid modes is primarily determined by g. However, by carefully selecting χ_{tr} to be moderate, one can access a straddling regime [81] in which the hybrid modes retain significant anharmonicity over a wider range of bare transmon frequencies, potentially increasing the number of mechanical qubits. Conversely, if χ_{tr} is too large, the transmon's second transition frequency $\omega_{e,f}$ is very detuned from the bare SAW mode frequencies, thereby limiting the effectiveness of the straddling regime. For the parameters used in Fig. 7, we find that $\chi_{\mathrm{tr}}/2\pi = -100$ MHz offers a good compromise.

APPENDIX C: EXPERIMENTAL DETAILS: DESIGN, FABRICATION, SETUP

1. Fabrication

The fabrication begins with a cleansing of an intrinsic semi-insulating gallium arsenide wafer (AXT Inc) in isopropanol (IPA).

a. Interdigital transducer (IDT)

The 2" GaAs substrate is spin-coated with a double-resist layer of 60 nm of methyl methacrylate (MMA) followed by 100 nm poly methyl methacrylate (PMMA). Both layers are baked at 180 °C for 5 min. The crystallographic direction [100] is aligned in the microscope with a precision of $\pm 0.5^\circ$, and mounted on the cassette of an E-beam lithography machine (Raith EBPG 5200). The IDTs are exposed with a beam of 2 nA and a base dose of 250 $\mu C/cm^2$, proximity error correction and with 20 nm negative bias on the fingers' width. After developing the resist in a solution of MIBK:IPA 1:1 for 60 s the wafer is blow dry with a nitrogen gun and exposed to 10 s oxygen plasma generated with 50 W of power (Plasma-Therm). The sample is loaded in the evaporation chamber of a Plassys evaporator and pumped overnight to reach a base pressure of 5×10^{-8} mBar. Following the evaporation of 30 nm thick layer of aluminum, the wafer is placed in a preheated beaker with Rem1165 at 85 C for 30 min and left in lift-off for additional 3 h. After the aluminum residues have been removed with a pipette, the wafer is transferred to a new beaker with Rem 1165 at 85 C for 5 min, followed by sonication at 40% power at 35 kHz for 3 min. The same operation is repeated after transferring the wafer to room-temperature methanol and finally to a beaker with room-temperature IPA.

b. Ground plane

The wafer is spin-coated with double-layer optical resist, 300 nm of LOR 3A, baked at 180C for 5 min and 500 nm of S1805, baked at 115C for 5 min. The resist is exposed with 97 mJ/cm^2, developed in MF319 for 60 s with a light manual agitation and rinsed with a deionized water gun for 2 min. After a light descum in oxygen plasma at 20 W for 20 s the wafer is loaded in Plassys evaporator where 150 nm of aluminum are deposited. For lift-off we follow the same procedure used for the IDT.

c. Josephson junctions

The wafer is spin-coated with double-resist layer comprising 400 nm of MMA and 400 nm of PMMA and both layers are baked at 180 C for 5 min. The exposure Manhattan junctions pattern is performed in the electron beam lithography (EBL) with a dose of 600 $\mu C/cm^2$, and is followed by a development of 60 s in a solution of MIBK:IPA 1:1 and a light descum in oxygen plasma at 50 W for 20 s. The wafer is loaded in a Plassys evaporator where 50 nm of aluminum is deposited at 45° angle, followed by a static oxidation at 2 mBar for 20 min. After rotating the wafer axially by 90°, another deposition of 110 nm of aluminum is performed. Before venting the loadlock, the wafer is left 10 min in 10 mBar oxygen atmosphere.

d. Patches

To patch the junctions and the IDT to the ground plane we coat, expose and develop the pattern with the same procedure followed for the junctions. In the evaporator the wafer is exposed to Argon milling at 400 V for 2 min, followed by an evaporation of 200 nm of aluminum and by an oxidation in 10 mBar atmosphere for 10 min. Finally the standard lift-off procedure is performed.

As a final remark, the fabrication of the measured sample was performed in October 2020. From measurements performed on nominally identical samples right after the fabrication, we noticed negligible ageing in the chip performance. However, holes of hundreds of μm^2, clearly visible by optical microscopy, appeared on the large aluminum ground-pad.

2. Measurement setup

The measurement setup is shown in Fig. 12. The sample is wire bonded with aluminum wires on a custom printed circuit board and glued on a copper sample holder using PMMA resist. The sample holder is thermally anchored to the mixing chamber plate of a LD Bluefors cryostat with base temperature $\approx$10 mK. The sample holder is isolated from its electromagnetic environment via a shield with three layers: copper, aluminum and cryoperm.

Measurement signals are generated using a Quantum Machines platform comprising an arbitrary waveform generator (OPX+) and a frequency converter (octave). The output lines 1 and 2 of the octave are connected to the device via respectively the port 3 (launcher IDT feedline) and port 1 (SQUID array resonator feedline input) with nominally 70 dB attenuation. The transmission through the SQUID array feedline is collected from port 2 of the device and is amplified by a HEMT LNF-LNC4 8C at the 4 K stage. The reflected SAW feedline signal is measured using a circulator LNF-CICIC4 8A, and is also amplified by a HEMT LNF-LNC4 8C at the 4 K stage. A Marki FLP-0490 4.9 GHz low-pass filter is used on the port 1 of the device. Two double-isolators LNF-CICIC4 8A are used between device and HEMT. The signal is further amplified at room temperature using an Agile AMT-A0284 amplifier, and demodulated and downconverted in the Quantum Machines system.

The flux line of the SQUID array is connected to two coaxial lines via a Mini-Circuits ZDSS-2R5G5G-S+ diplexer, with each line including 30 dB of attenuation. A high-frequency line with a Mini-Circuits VHF-6010+ high-pass filter is used to apply the two-photon parametric drive. A low-frequency line with a Mini-Circuits VLFX-225+ low-pass filter is connected but not used in this work. An additional 10 dB of attenuation is inserted between the device and the diplexer to damp standing-wave modes.

Throughout this work, the bare frequency of the SQUID array is controlled using a superconducting coil attached

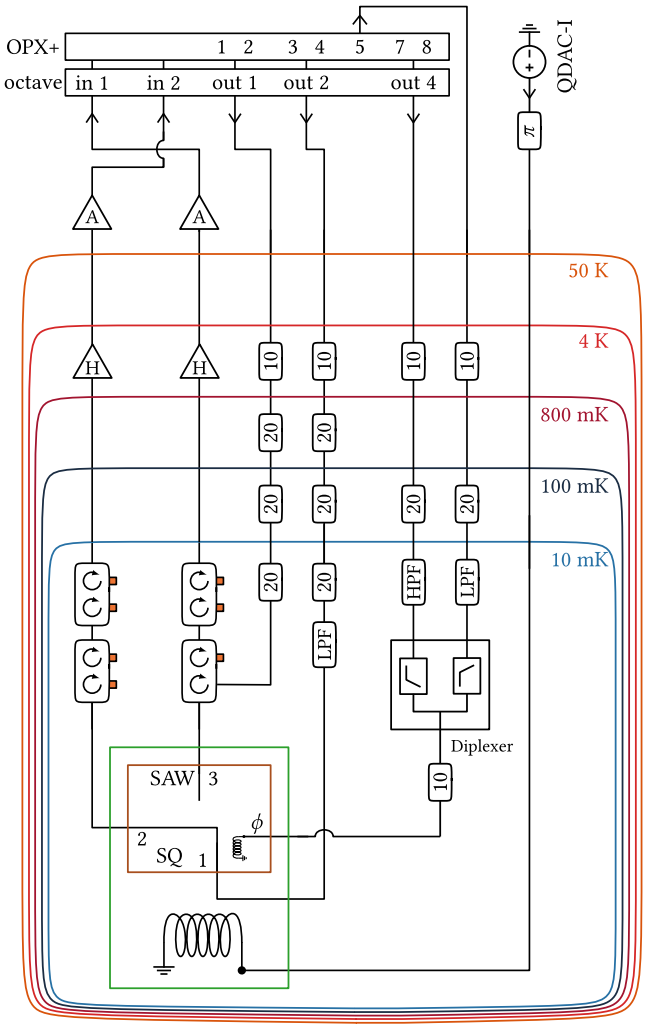


FIG. 12. Room-temperature measurement setup and cryostat wiring and filtering. Representative measurement setup used in cooldown 20251031CD. Minor changes performed in the other cooldowns are described in Sec. C 3.

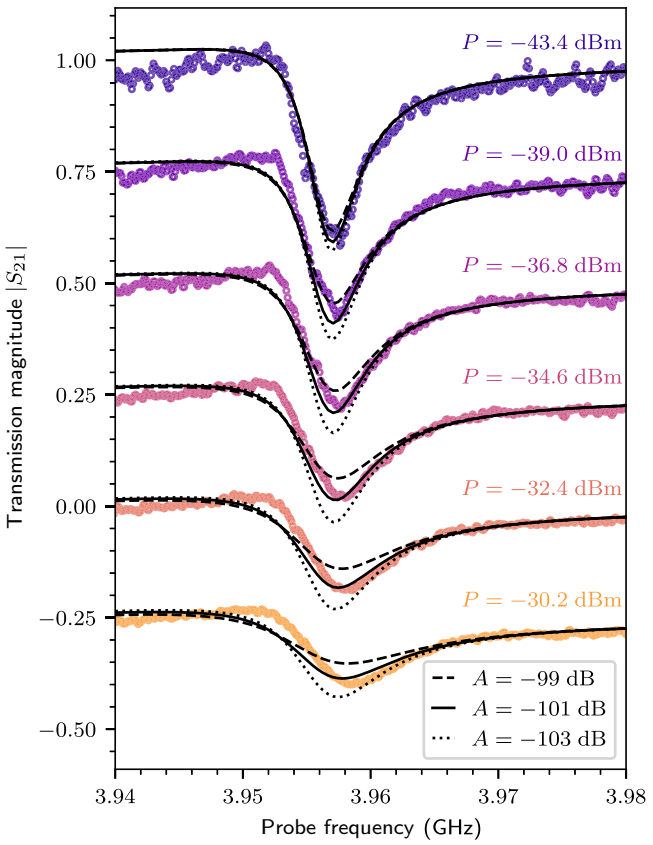


FIG. 13. Input line attenuation calibration. We perform a power sweep on a different device to calibrate the attenuation in the input line of the SQUID array resonator (port 1). The device is a Kerr resonator with nonlinearity exceeding its total dissipation rate studied in another work (device $N = 10$ in Ref. [66]). The colored markers indicate the magnitude of S_{21} measured for different powers P indicated at instrument level outside of the cryostat. Each S_{21} trace is shifted along y-axis by -0.25. We use the method described in Ref. [66] and fit the power sweep to a master equation model using QuTiP [92]. We find an attenuation of -101 ± 1 dB (black solid line). Dashed and dotted black lines indicate simulation results with ± 2 dB attenuation difference and show a worse agreement with the measurements.

on the bottom of the sample holder. We use a QDevil QDAC-I voltage source with a 1 kΩ low-pass π-filter with 30 Hz cutoff frequency to apply direct current in the coil.

3. Attenuation estimation

The measurement data reported in this work were measured across several CDs. In one cooldown (CD 20241206), we performed a calibration of the input attenuation line of the SQUID array resonator (port 1) using another device connected on a shared cryogenic switch at the mixing chamber stage of the cryostat. It is a Kerr resonator in the quantum regime, i.e., with nonlinearity larger than dissipation. The nonlinearity is known from the measurement of multiphoton transitions at high probe power [66]. We fit the power sweep shown in Fig. 13 with the input attenuation as the only free parameter. The Kerr resonator device and input power calibration method are explained in greater details in Ref. [66]. This allows us to find the self-Kerr χ_{SQ} of the SQUID array resonator presented in this work as reported in Fig. 5. The input line connected to port 3 (launcher IDT) is nominally identical to the one connected to port 1. We determine the attenuation of the launcher IDT input line by using the attenuation calibrated for port 1, accounting for difference in filtering and cabling at the mixing chamber stage of the cryostat using nominal room-temperature values for the different microwave components.

We recalibrate the attenuation of the input lines for all the other cooldowns, according to the following procedure:

CD 20241206; During this cooldown, port 1 (input of the SQUID array resonator feedline) is connected on the

same switch as the Kerr resonator [66]. The input attenuation is calibrated using the method described above, and we find $A_3{}^{SQ} = (-101 \pm 1)$ dB.

In the other cooldowns, no switch was used on the SQUID array resonator input (port 1), and the estimate of the attenuation of the input lines is based on the calibration performed during CD 20241206, given that the lines are nominally the same.

CD 20240913; We estimate the attenuation in the launcher IDT feedline by subtracting the nominal room-temperature attenuation of the additional components used in CD 20241206, namely

(a) one Marki LPF 4.9 GHz filter (0.7 dB),
(b) one RLC Electronics F-30-8000 (0.7 dB),
(c) one Radiall r591723605 switch (0.3 dB),
(d) extra cabling (0.5 dB).

Moreover, in CD 20241206 an extra 20 dB internal attenuation is applied in the measurement instrument. On the whole, we estimate a difference in attenuation of 22.2 dB, which we add to A_3^{SQ} to obtain $A_1^{IDT} = (-78.8 \pm 2.0)$ dB, where the increased error accounts for the misestimation of the attenuation of the different components.

Similarly, we estimate the attenuation of the different components on the SQUID array resonator feedline, finding $A_1^{SQ} = (-78.8 \pm 2.0)$ dB.

CD 20240927; Here, to calibrate the input attenuation of the SQUID array resonator line, we perform a power sweep of the SQUID array resonator near zero flux. Then, we simultaneously fit several S_{21} traces for increasing power, assuming the value of self-Kerr of the bare SQUID array resonator obtained from the cross-Kerr study (Fig. 5). We find an attenuation $A_2^{SQ} = (-97.0 \pm 1.5)$ dB, where the increased error accounts for the nonidealities in the calibration process.

Finally, we obtain the attenuation of the feedline of the IDT by estimating the attenuation of the different components compared to the SQUID array resonator line. The launcher IDT input line has one extra circulator (LNF-CICIC4 8A, 0.2 dB) and some extra cabling (0.5 dB). The SQUID array feedline has an additional low-pass filter (MARKI FLP-0490, 0.7 dB). Thus, we estimate the attenuation on the IDT feedline to be $A_2{}^{IDT} = (-97 \pm 2)$ dB, where the increased error accounts for the misestimation of the attenuation of the different components.

CD 20250214; we apply the same protocol as in CD 20240927. We find $A_4{}^{SQ} = (-102.0 \pm 1.5)$ dB for the feedline of the SQUID and $A_4{}^{IDT} = (-103.6 \pm 2.0)$ dB for the feedline of the IDT.

The attenuation values estimated in the different cooldowns are summarized in Table III.

Additional measurements applying two-photon drive to the SQUID array flux line were performed in a later cooldown, **CD 20251031**. The parametric drive is applied via the flux line, and no calibration of input attenuation was performed.

APPENDIX D: MEASUREMENT DETAILS

1. Bare surface acoustic waves

a. Dissipation analysis

The SAW modes come in pairs, with one longitudinal and one transverse mode. Longitudinal modes are strongly coupled to the launcher IDT, which translates into larger κ_{ext}. The transverse modes have smaller κ_{ext} and larger κ_{int}. For convenience, we indexed all modes so that odd numbers are for longitudinal modes and even numbers are for transverse modes.

We characterize the bare SAW modes by setting the SQUID array resonator frequency far detuned from the SAW modes, for example, at zero-flux bias for which $\omega_{SQ}/2\pi \approx 4.7$ GHz. We measure the reflection signal S_{33} using the setup reported in Fig. 12 to obtain the SAW modes bare frequencies and dissipations.

In Fig. 2 of the main text, we only report the longitudinal modes that we could resolve from port 3 (launcher IDT). In Fig. 14 we also report the parameters of the transverse modes extracted from port 3 (blue and blue-green markers).

In addition, we could also identify 11 extra SAW modes by flux tuning the SQUID array resonator across the SAW modes, and measuring ports 1 and 2 (S_{21} measurements, see Fig. 3). These SAW modes are coupled to the SQUID array resonator but are not coupled to the launcher IDT. The difference in coupling is due to the different placement of the launcher and coupler IDTs along the Bragg mirror. We do not have a direct access to the dissipation rates of these extra dark modes. We set their total dissipation rates to the average of the other longitudinal (95 kHz) or transverse modes (326 kHz), shown as gray markers in Fig. 14. These values are used in Eq. (5) to perform the global fit of κ_{SQ} in Fig. 4.

b. SAW mode spacing (FSR)

The FSR of the SAW resonator is approximately equal to 8.6 MHz, and it is determined by the effective cavity length, L_c. The FSR is shown in Fig. 15. Longitudinal SAW modes are separated by 8.25 to 8.8 MHz, with the largest deviation on the edge of the mirror bandwidth due to increasing effective cavity length [16]. The transverse modes have a resonance frequency from 1.6 to 2.15 MHz higher than the longitudinal modes [60].

c. FEM simulations of modes spacial profile

An ideal SAW resonator confines the mechanical excitation along the direction of propagation, between two Bragg mirrors. However, excitations with different mode profiles that have a small transverse propagation component are

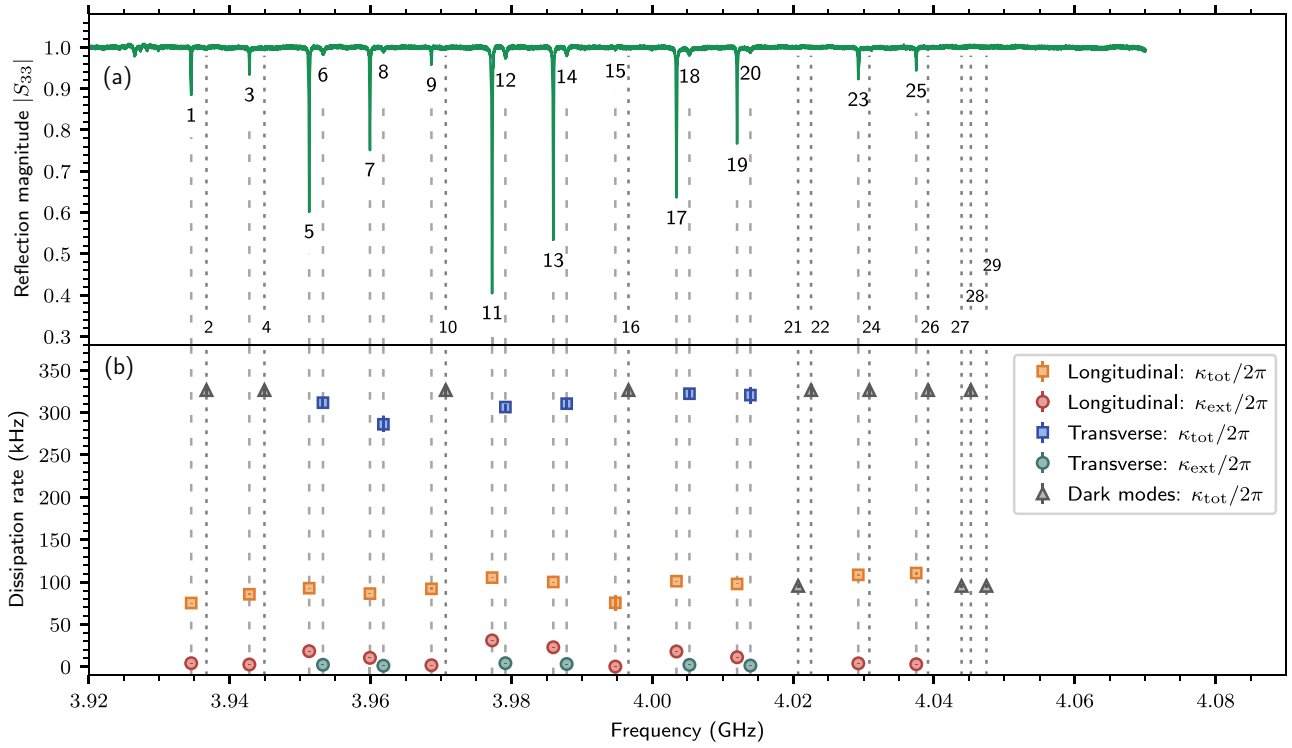


FIG. 14. Frequency and dissipation rates of bare surface acoustic wave modes. (a) Same trace S_{33} shown in Fig. 2. The SQUID array resonator is set to zero-flux point with frequency 4.7 GHz. (b) In Fig. 2 we only reported the parameters of longitudinal surface acoustic wave modes measured from the launcher IDT side (S_{33}). Here, we also report the parameters of transverse surface acoustic wave modes (blue square and blue-green circle markers) with larger internal dissipation rates. Other surface acoustic wave modes could be identified only from the SQUID array resonator side (S_{21}). We set their dissipation rates to the average value of the other modes that we could resolve directly (gray triangle markers). We use these parameters of the bare surface acoustic wave modes throughout the rest of the articles. The power of the probe tone at device level was −131 dBm.

also weakly confined and can be excited by the IDT due to its finite lateral dimensions.

Due to their mode profile, the transverse mode shows a smaller coupling to IDT and a slightly larger frequency compared to the longitudinal one. Finite element method simulations can be used to study such behavior; however, the full simulation of our geometry is very resource-intensive and is out of the scope of this work. Nevertheless, the simulation of a unit cell of the launcher (or coupler) IDT can be used to show the spatial profiles of the transverse modes.

In Fig. 16, a single finger pair with split geometry and periodic boundary conditions is used to simulate an IDT launcher. The mesh reported in panel (a) has been chosen to render every element's spatial extension smaller than the wavelength. The colorcode represents the displacement perpendicular to the substrate. In panel (b), a longitudinal mode is found at a frequency of 3.986 GHz and presents a spatial profile with a maximum at the center of the finger pair (see panel c). Higher frequency modes show a profile with one or multiple nodes, characteristic of the transverse modes. Such simulations agree qualitatively with the physical imaging of such modes on GaAs [60].

d. Dissipation versus power

We investigate the dependence of the dissipation of the bare SAW modes on the power of the input field. This measurement was performed with a vector network analyzer during the last cooldown reported in Table III. The attenuation of the line is obtained by fitting a power sweep of the SQUID array, as detailed above Sec. C 3. As shown in Fig. 17, the total dissipation decreases for increasing power, typical of the saturation of spurious two-level systems. The red dashed line corresponds to the power at which the trace shown in the main text Fig. 2 and in Fig. 14 was acquired.

e. Mechanical dissipation limitation

The propagation of SAW in anisotropic media is affected by beam steering, where the propagation direction is not perpendicular to the wave front. In a finite-size resonator, this limits the quality factor to [97]

$$Q_{\mathrm{dif}} = \frac{5\pi}{1+\gamma}\frac{W^2}{\lambda^2}, \tag{D1}$$

where W is the width of the IDT launcher.

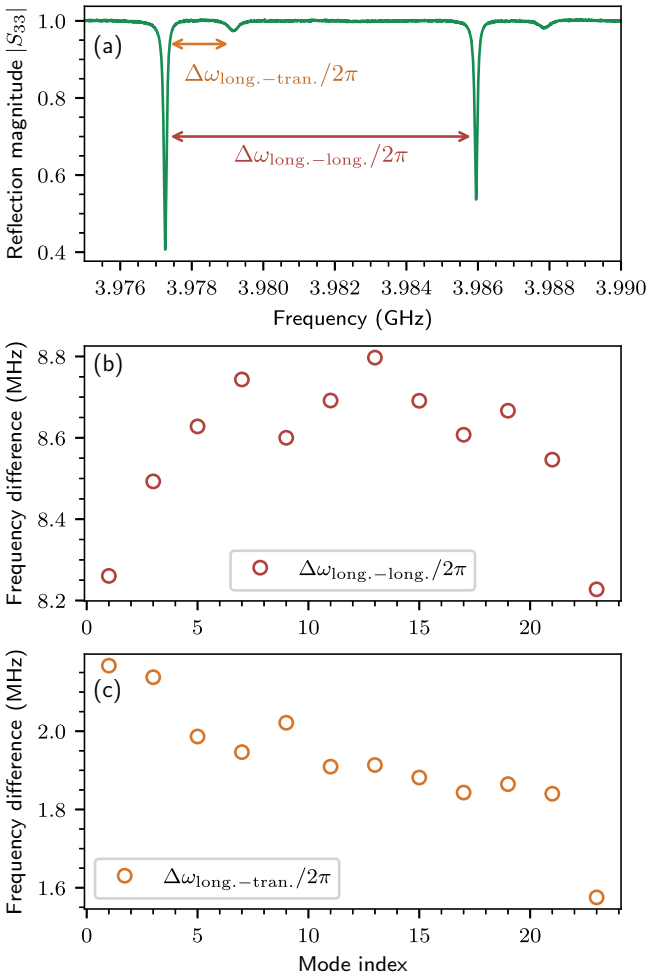


FIG. 15. Frequency difference between surface acoustic wave modes. (a) Zoom-in on the trace S_{33} of bare surface acoustic wave modes reported in Fig. 2(a). (b) and (c) From the surface acoustic wave mode positions shown in Fig. 14, we compute the frequency difference between neighboring longitudinal surface acoustic wave modes (b) and between a longitudinal mode and its neighboring transverse mode (c).

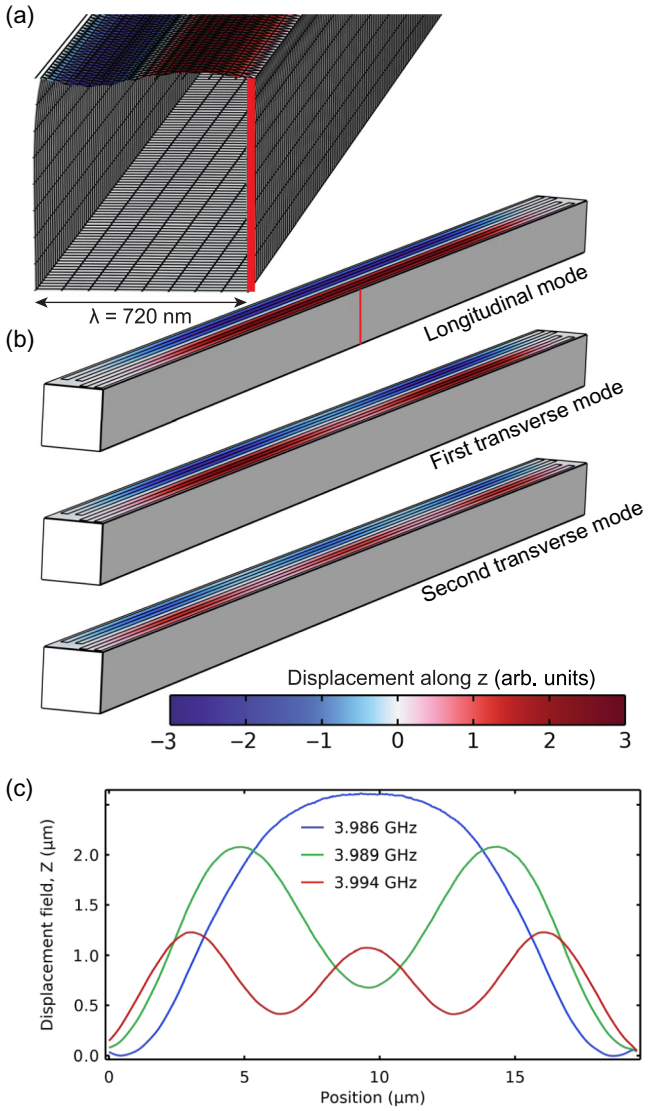


FIG. 16. Spatial profile of longitudinal and transverse modes. Finite element method simulation of the displacement in the z direction, produced by an interdigital transducer with a 1 V. In (a) a section in the center of the finger pairs show the displacement increased by a factor of 100 and the meshing elements on the surfaces. In (b) the applied voltage to each finger pair is at frequencies of 3.986, 3.989 and 3.994 GHz, exciting longitudinal, first and second transverse modes, respectively. (c) A line cut along the finger length on the surface shows the displacement for the different frequencies.

The beam steering factor γ depends on the alignment of the IDT and mirror with the propagation direction along the crystal axis [98]. We believe that the error in fabrication arises during the alignment procedure with the wafer flat. From previous devices realized on GaAs [28] and the one we realized here, we estimate $\gamma \approx -0.75 \pm 0.05$. As shown in Fig. 16, the quality factor saturates at high power to this ultimate level. We design our resonator to host a transmon qubit with the correct dimensions. Therefore, we believe that Q around 100 thousand (dissipation around 50 kHz) is the limit for this device. Future devices, with a larger aperture, can have a higher mechanical quality factor.

However, at low photon numbers, the quality factor degrades due to TLS losses. Introducing a better cleaning process will bring the quality factor closer to the diffraction limit.

2. SQUID array dissipation

a. Acoustic relaxation rate

Outside the Bragg mirror stopband, the acoustic relaxation rate of the SQUID array resonator is given

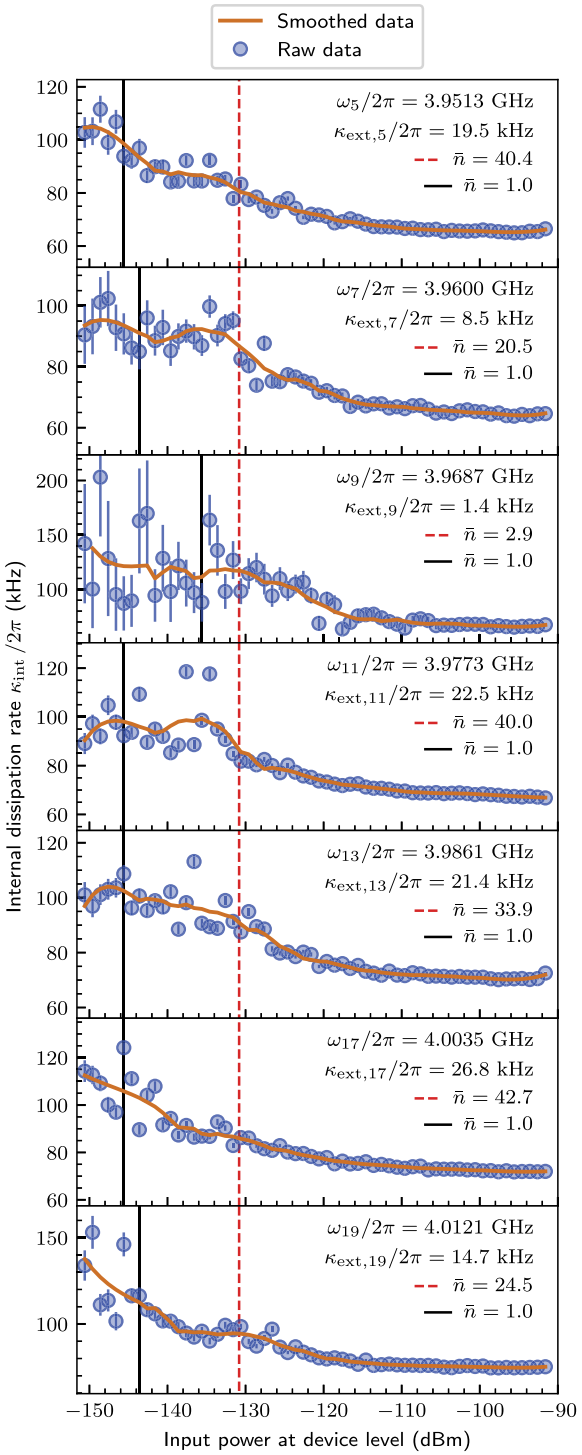


FIG. 17. Internal dissipation rate of surface acoustic wave modes as a function of input power. We measure S_{33} for increasing probe power and extract the dissipation rates by fitting each surface acoustic wave mode. Dissipation rates extracted are shown with blue markers, and the trend smoothed with a Savgol filter is shown with a solid orange line. External dissipation rates do not depend on power, and we report their values in each subplot. The input power is converted to average phonon number $\bar{n}$. The power corresponding to $\bar{n} = 1$ is shown with solid black lines, and the power used in Fig. 2 with dashed red lines.

by [45,97]

$$\Gamma(X) = \frac{1.3}{2\sqrt{2}} K^2 N_p^{\mathrm{coupler}} \omega_0^c \left(\frac{\sin X}{X}\right)^2, \tag{D2}$$

where $K^2 = 0.07\%$ is the effective electromechanical coupling in GaAs, $N_p^{\mathrm{coupler}} = 14$ is the number of split-finger pairs in the coupler IDT, and $X = \pi N_p^{\mathrm{coupler}}(\omega - \omega_0^c)/\omega_0^c$, with $\omega_0^c/2\pi$ the central frequency of the SAW cavity and $\omega/2\pi$ the frequency of the electromagnetic mode. In our case, the coupling results in approximately $\Gamma/N_p^{\mathrm{coupler}} \approx 2\pi \cdot 1.3$ MHz per split-finger pair.

b. SQUID array dissipation measurement

We report here the measured dissipation rates of the SQUID array resonator as a function of the bare SQUID array resonator frequency, changed via magnetic flux generated by an external superconducting coil. This measurement is performed using a vector network analyzer. For each flux value, we measure S_{21} and fit it to Eq. (B18) to obtain internal and external dissipation rates. The results are shown in Fig. 18.

The external dissipation rate of the SQUID array resonator is determined by the capacitive coupling to the $Z_0 = 50\ \Omega$ feedline. The frequency of the SQUID array resonator is tuned by changing the effective Josephson inductance using magnetic flux. We thus expect that when changing the resonance frequency of the SQUID array resonator, its external coupling rate scales as

$$\kappa_{\mathrm{ext,SQ}} = \frac{C_c^2}{C_{\mathrm{tot}}} Z_0\, \omega_{\mathrm{SQ}}^2 = \tau\, \omega_{\mathrm{SQ}}^2, \tag{D3}$$

where C_c is the coupling capacitance and C_{tot} the total capacitance of the SQUID array resonator. The solid green line in Fig. 18 follows this formula with a value of $\tau = 0.31$ ps chosen to match the measured external dissipation rate around the mirror bandwidth.

Ripples in dissipation rates are observed for $\omega_{\mathrm{SQ}} > 4.2$ GHz. External dissipation rate is increased near 4.4 GHz and 4.6 GHz, while internal dissipation rate seems to increase near 4.55 GHz and 4.7 GHz. The origin of these ripples might be related to the presence of standing waves from spurious modes in the electromagnetic environment.

The internal dissipation rate can originate from two mechanisms. First, we estimate the spurious internal loss rates to be roughly constant from 3.6 GHz to 4.3 GHz with about $\kappa_{\mathrm{int}}^{\mathrm{extra}}/2\pi \approx 2$ MHz. Second, the SQUID array can emit phonons in the substrate via the coupler IDT at its capacitive end. This coupling Γ varies with the frequency following a sinc^2 profile as detailed in Eq. (D2). However, the Bragg mirrors open a gap in the phonon continuum of the substrate. Therefore, we expect this second emission channel of the SQUID array to be suppressed inside the

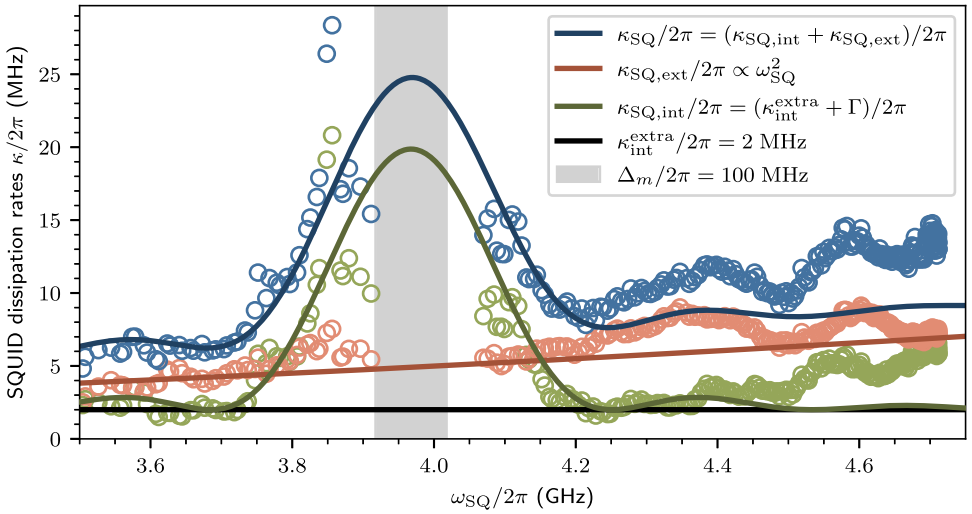


FIG. 18. Dissipation of SQUID array versus flux. We sweep the flux threading the SQUID array resonator, measure S_{21} and fit the traces with Eq. (B18) to extract the dissipation rates. Extracted values of internal (green), external (orange) and total (blue) dissipation rates are shown with markers. The internal dissipation rate from phonon emission via the coupler interdigital transducer [Γ, Eq. (D2)] is enhanced near the central frequency of the surface acoustic wave cavity $\omega_0^c/2\pi \approx 3.967$ GHz. Additional internal losses are estimated to be approximately constant at $\kappa_{int}^{extra}/2\pi \approx 2$ MHz near the mirror bandwidth (black line). SQUID array dissipation cannot be directly measured within the mirror bandwidth (gray shaded region astride $\omega_0^c/2\pi$). The power of the probe tone was -142 dBm, corresponding to an average photon population in the SQUID array of $\bar{n}_{SQ} = 0.08$.

mirror stop band (gray shaded region in Fig. 18), except at the frequency of the bare cavity modes [16].

3. Superstrong coupling criterion for an uneven spectrum

The usual superstrong coupling regime criterion $g \gtrsim \Delta\omega$ presumes a uniform free spectral range. In our device, the spectrum is uneven: longitudinal and transverse manifolds interleave, producing local spacings that alternate between ≈ 2 MHz and ≈ 6.5 MHz. In addition, the coupler IDT is placed at approximately one-third of the cavity length, so the spatial overlap (and thus g_i) oscillates with mode index, strongly suppressing roughly every third longitudinal mode.

To enable a well-posed comparison in an uneven spectrum, we report two local, mode-resolved ratios:

(1) Mode-based ratio [one value per bare mechanical mode i, Figs. 19(a) and 19(b)]:

$$R_i \equiv \frac{g_i}{\overline{\Delta\omega i}}, \quad \overline{\Delta\omega i} = \left[(\omega_i - \omega_{i-1}) + (\omega_{i+1} - \omega_i)\right]/2. \tag{D4}$$

(2) Pair-based ratio [one value per hybrid mode i connecting adjacent bare modes $i, i+1$, Figs. 19(c) and 19(d)]:

$$\tilde{R}_i \equiv \frac{\bar{g}_i}{\Delta\omega_i}, \quad \bar{g}_i = \tfrac{1}{2}\left(g_i + g_{i+1}\right), \quad \Delta\omega_i = \omega_{i+1} - \omega_i. \tag{D5}$$

In our device, $\overline{\Delta\omega_i}$ alternates between approximately 2 and 6.5 MHz with an average near 4 MHz. Consequently, R_i tracks the coupling envelope: strongly participating modes yield $R_i > 1$, while modes suppressed by the IDT placement give $R_i < 1$. The pair-based ratio $\tilde{R}_i$ tends to exceed unity for pairs with small $\Delta\omega_i$. As shown in Fig. 19, depending on the chosen metric, several modes have superstrong ratios exceeding unity ($\approx$ 7–8 in our dataset). Moreover, the average superstrong ratios are just slightly below one, consistent with operation at the onset of multimode (superstrong) coupling regime.

4. Hamiltonian parameter extraction

We perform a global fit of the linear RWA Hamiltonian (B14) to the resonant flux sweep shown in Figs. 3(b) and 3(c). Namely, for each flux value we extract the frequency of the resolved eigenmodes for both S_{21} and S_{33} traces. The loss function is computed globally over the entire 2D map, using the difference between the minima extracted and the eigenvalues predicted by the numerical diagonalization of the matrix T [Eq. (B3)]. The free parameters of the fit are the frequencies of the 11 SAW modes which cannot be resolved from the spectroscopy (gray markers in Fig. 14), together with the 29 coupling strengths between the electromagnetic and mechanical modes, g_i.

The fitting protocol is performed iteratively in two steps: a first general fit is performed over the full bandwidth of the mechanical cavity, as shown in Fig. 3, and then a second fit is implemented over a narrower region across the

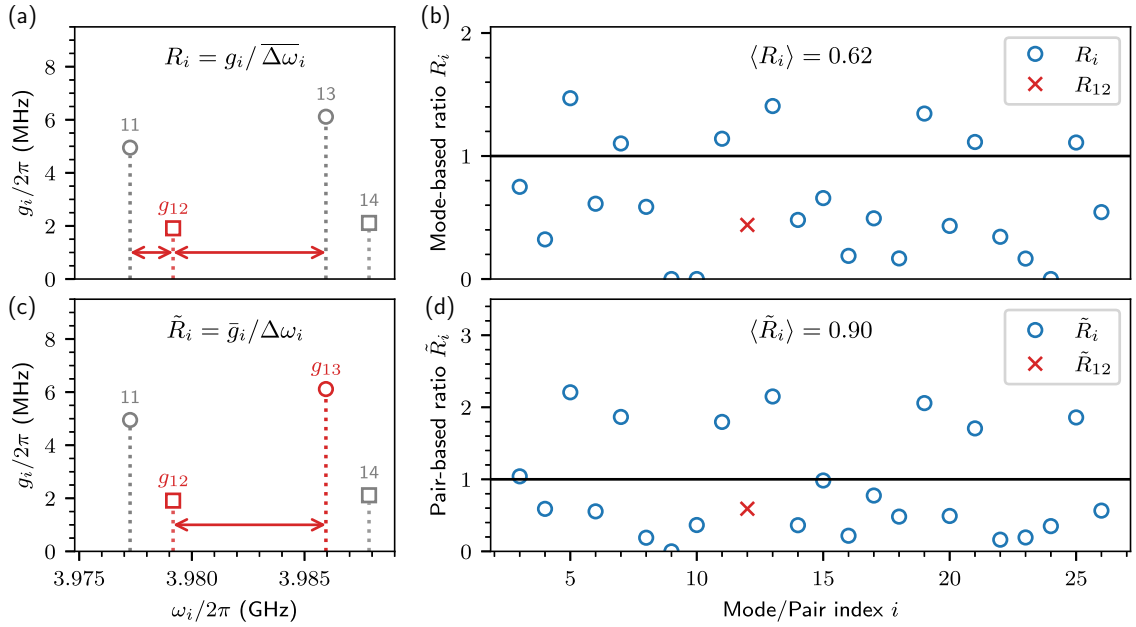


FIG. 19. Two local metrics for superstrong coupling in an uneven spectrum. (a) and (b) Mode-based ratio R_i: ratio of the surface acoustic wave-SQUID coupling g_i for bare mode i to the local average spacing $\overline{\Delta\omega_i} = \left[(\omega_i - \omega_{i-1}) + (\omega_{i+1} - \omega_i)\right]/2$. (c) and (d) Pair-based ratio $\tilde{R}_i$: ratio of the average coupling $\bar{g}_i = (g_i + g_{i+1})/2$ to the adjacent-mode spacing $\Delta\omega_i = \omega_{i+1} - \omega_i$. Red crosses in (b) and (d) mark the ratios for the modes/pairs highlighted in red in (a) and (c). Average values for each metric, $\langle R_i \rangle$ and $\langle \tilde{R}_i \rangle$, are indicated in (b) and (d), respectively.

bare SAW modes $[\omega_8; \omega_{16}]$. The second fitting step aims at refining the extraction of the parameters for the participation and the dissipation studies presented in Fig. 4. In the refined fit, the free parameters are the frequency of mode b_{16} (dark form port 3) and all the coupling strengths $[g_8; g_{16}]$. Finally, to keep consistent numbering between bare and hybridized modes, we set the couplings of the bare SAW modes b_9, b_{10}, b_{24} to zero.

5. Derivative and dissipation of hybridized modes

a. Additional data derivative and dissipation

The protocol to extract the participation of the SQUID array resonator from the derivative of the measured frequency of the hybrid modes is applied to the six hybrid modes in the range from c_{10} to c_{15}. The two bare SAW modes b_9 and b_{10} have vanishing coupling to the SQUID array resonator, $g_9 = g_{10} = 0$. Therefore, the three hybrid modes c_8, c_9 and c_{10} appear as a single continuous mode. It is the pumped mode c_p shown with pink dotted lines in Fig. 5(a), and in this section we refer to it as c_{10} for simplicity. The extended data set of Fig. 4 is displayed in Figs. 20(a), 20(c), 20(e), and 20(g), showing good agreement both from reflection and transmission data, in blue and green respectively. Modes with maximum participation below 2 % are shown as solid gray lines. The analysis of the dissipation is reported in Figs. 20(b), 20(d), 20(f), and 20(h), where the solid black line is the result of the simultaneous fit to Eq. (5) over all the modes under study, including the ones shown in Fig. 4.

A more comprehensive model of the total dissipation rate of the hybrid modes would account for interference between the external coupling rates of the bare SAW modes to the IDT, as detailed in Ref. [64]. However, in our device, the total dissipation rate of the bare SQUID array resonator is around two orders of magnitude higher than the one of the bare SAW modes. Therefore, when modes are hybridizing, their dissipation rate $\tilde{\kappa}$ is dominated by the bare SQUID array resonator contribution, so we can safely neglect possible interference effects.

The error reported on the value of κ_{SQ}, extracted from the simultaneous fit, is increased to account for the uncertainty on the participation ratios, $|u_{ij}|^2$, computed from the electromechanical coupling strengths g_i and the frequency of the bare SAW modes ω_i.

b. Extra spurious peak

We observed several weakly coupled spurious modes. To accurately extract the participation ratio of the SQUID array resonator based on the derivatives of the hybrid modes, we first characterized how the SQUID array resonator couples to these spurious modes. These modes do not follow the pattern of longitudinal and transverse modes reported in Fig. 14. These spurious modes are possibly associated with higher-order transverse excitations and appear as small avoided crossings, as shown in

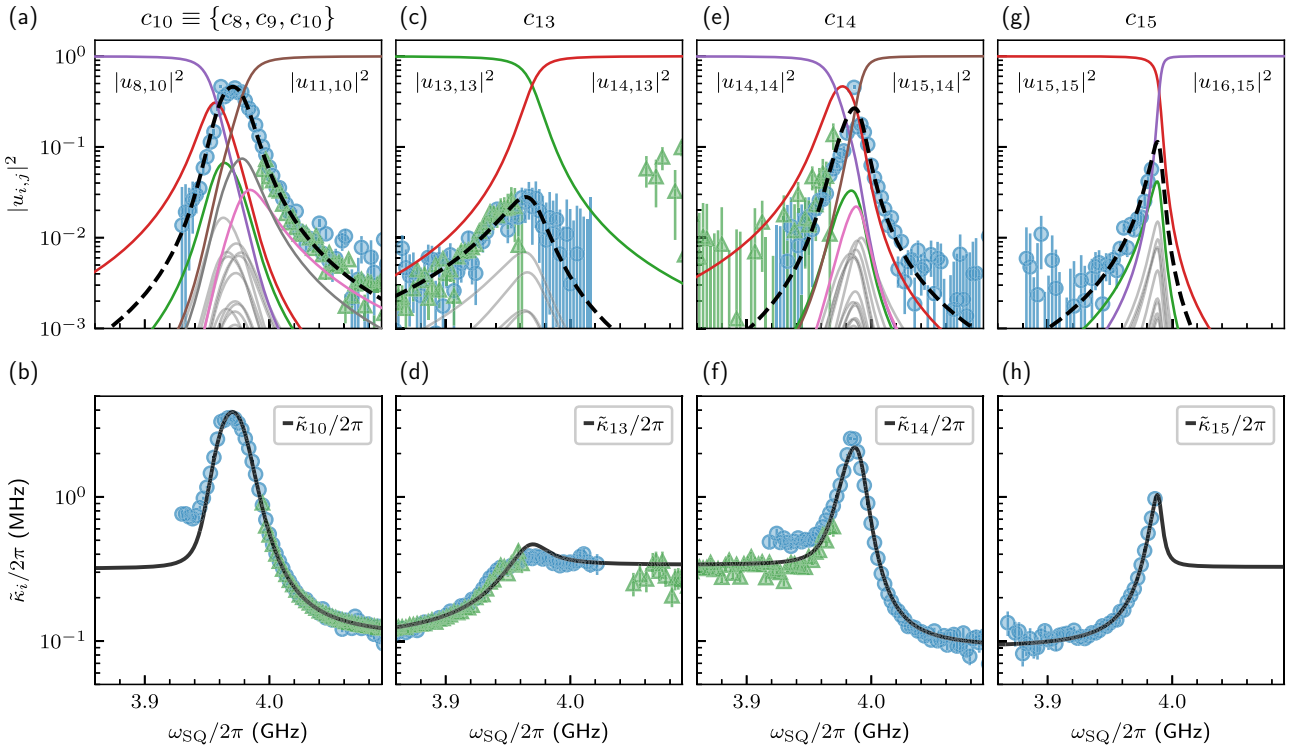


FIG. 20. Additional data for Fig. 4. Bare modes participation ratios (top row) and total dissipation rates (bottom row) for four additional hybridized modes, $\{c_{10}, c_{13}, c_{14}, c_{15}\}$. The analysis is performed on the same detailed flux sweep as shown in Figs. 4(a), 4(b).

Figs. 21(a) and 21(b) for the hybrid mode c_{12}. To track the position of these features, we fit the spectrum at each bare SQUID array resonator frequency using a double Lorentzian model,

$$L_1(\omega) + L_2(\omega) = \frac{A_1}{1 + \left(\frac{\omega - \omega_{r,1}}{\sigma_1}\right)^2} + \frac{A_2}{1 + \left(\frac{\omega - \omega_{r,2}}{\sigma_2}\right)^2}, \tag{D6}$$

where A_i are normalization factors, $\omega_{r,i}$ are the resonance frequencies, and σ_i are the half-widths at half-maximum for each Lorentzian. The coupling between the SQUID array resonator and the spurious mode is estimated by applying the same fitting protocol detailed in Sec. D 4 to the frequency of the two resonances extracted from the double Lorentzian fit, which yields $g_{spurious}/2\pi \approx 0.8$ MHz. Then, we take the derivative of the position of the resonance frequency of each Lorentzian with respect to the bare SQUID array resonator frequency [blue diamonds and crosses in Fig. 21(c)]. We find good agreement with the participation of the SQUID array resonator extracted from the numerical diagonalization of the linear model complemented with the extra peaks (orange lines).

In practice, we always use the single-peak model to extract the dissipation of the hybrid modes. However, when the data can be successfully fit with a two-peak model [see Eq. (D6)], the single-peak model fails to provide an accurate dissipation value. In these cases, we exclude the corresponding data from our dissipation analysis and use the results of the two-peak fit solely to define the exclusion regions. This procedure prevents overestimation of dissipation, as indicated by the gray markers in Fig. 21(d).

6. Self-Kerr measurements

The protocol to measure the self-Kerr of the hybrid modes consists in a resonant single-tone power sweep across the modes of interest. In Fig. 22, the self-Kerr map of the hybrid modes c_{10} to c_{15} is compared to the simulation of a driven classical Duffing oscillator as a function of the amplitude of the drive [66,68]. In the simulation all the parameters are fixed, and in particular the self-Kerr inherited by the SAW modes is derived from Eq. (6b). The theoretical curves of the model qualitatively capture the displacement of the SAW modes, until either two SAW modes start to repel each other or the mode enter the metastable region shown by the yellow and orange markers.

7. Cross-Kerr measurements

a. Measurement protocol

Cross-Kerr coefficients, $\tilde{\chi}_{i,j}$, are a quadratic correction to the linear model, which quantifies the shift in the

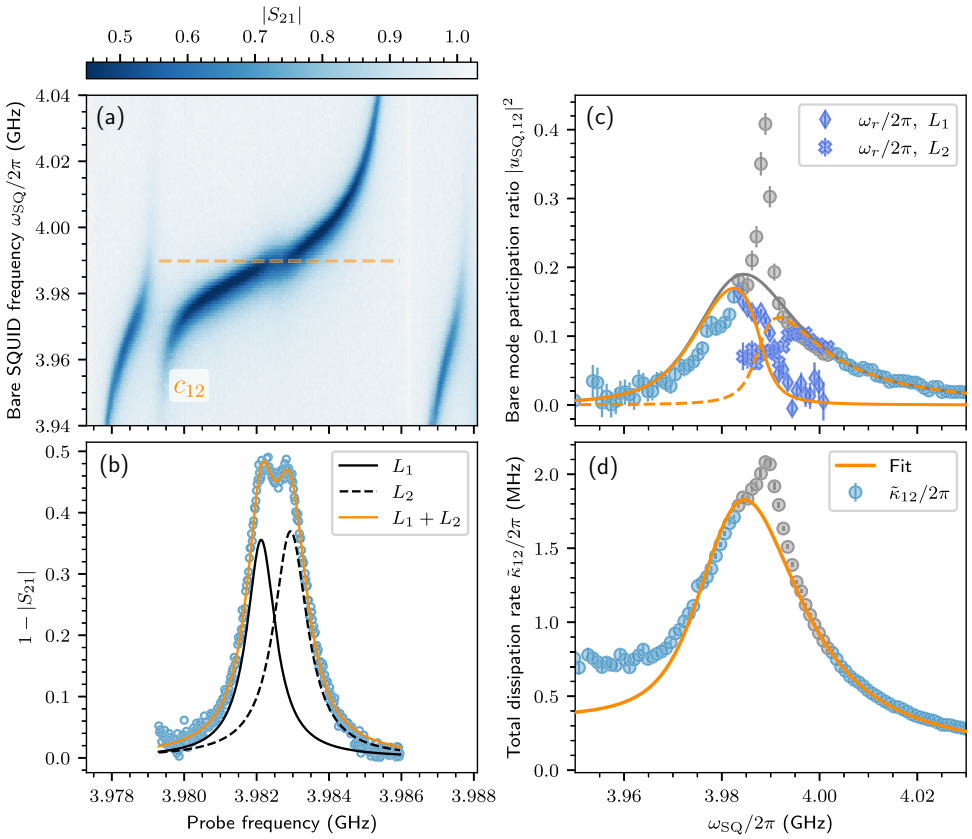


FIG. 21. Mode participation and dissipation rate analysis in presence of a spurious surface acoustic wave mode. (a) Zoom-in view of the flux sweep shown in Fig. 4(a), highlighting the presence of an additional SAW mode of bare frequency ≈ 3.983 GHz. (b) We report $1 - |S_{21}|$ at the bare SQUID array resonator frequency $\omega_{SQ}/2\pi = 3.99$ GHz [orange dashed line in (a)], where the hybrid mode c_{12} is maximally hybridized with the spurious SAW mode. Measurement data are shown as blue markers. The data are fit to a double Lorentzian model [Eq. (D6)], yielding the solid orange line. The individual Lorentzian curves L_1 and L_2 are shown as black solid and dashed lines, respectively. (c) Participation of the bare SQUID array resonator in the hybridized mode c_{12} and spurious mode. Simulated participation ratios are shown for the case without the spurious mode (gray solid line) and with the spurious mode included (orange solid and dashed lines). The SQUID array resonator participation ratio is also obtained from the derivative of the measured eigenfrequencies [Eq. (4)]. Circle markers come from the same protocol described in Fig. 4, which fails in the presence of a spurious surface acoustic wave mode (gray markers). Cross and diamond blue markers are obtained from the derivative of the position of Lorentzians L_1 and L_2. (d) Dissipation rate of hybridized mode c_{12}. Circle markers are obtained from measured S_{21} using the protocol of Fig. 4. The dissipation is overestimated in the double peak region (gray) compared to the solid orange line reporting the result of the global fit of the total dissipation rates of the hybrid modes [Figs. 4(d) and 4(f)].

frequency of hybrid mode c_i as a function of the average number of excitations in hybrid mode c_j. The protocol that we adopted for measuring cross-Kerr coefficients consists of two-tone spectroscopy measurements, where we apply a pump tone on mode c_j and a weak probe tone on c_j [99]. The need to sweep the pump tone arises from the self-Kerr nonlinearity acquired by the hybrid modes, which induces a power-dependent frequency shift also in the pumped mode. As the pump power increases, this shifts the pumped mode out of resonance, necessitating an adjustment of the pump frequency to maintain resonance condition.

For every couple of hybrid modes, the dependence of the cross-Kerr on the bare SQUID array resonator frequency is obtained by first sweeping the power of the pump tone and then the flux bias applied via the external coil. For instance, the sequence in Figs. 23(b)–23(h) expands the two-tone spectroscopy map for the couple of hybrid modes (c_{12}, c_p) shown in Fig. 5(b). For this power sweep, the SQUID array resonator frequency is marked by the red dotted line in Fig. 23(a).

For the sake of simplicity, in the cross-Kerr study, we adopt the notation $c_p \in \{c_8, c_9, c_{10}\}$, since the bare modes b_9 and b_{10} are included in the numbering, but do not contribute effectively in the model as their coupling is set to zero, $g_9 = g_{10} = 0$.

Finally, the external and the total dissipation rates of the hybrid modes vary significantly as a function of the frequency of the bare SQUID array resonator. Therefore, we calibrate the power of the pump tone so that the excitation number in the pumped mode remains $\lesssim 10$ for any ω_{SQ}. In

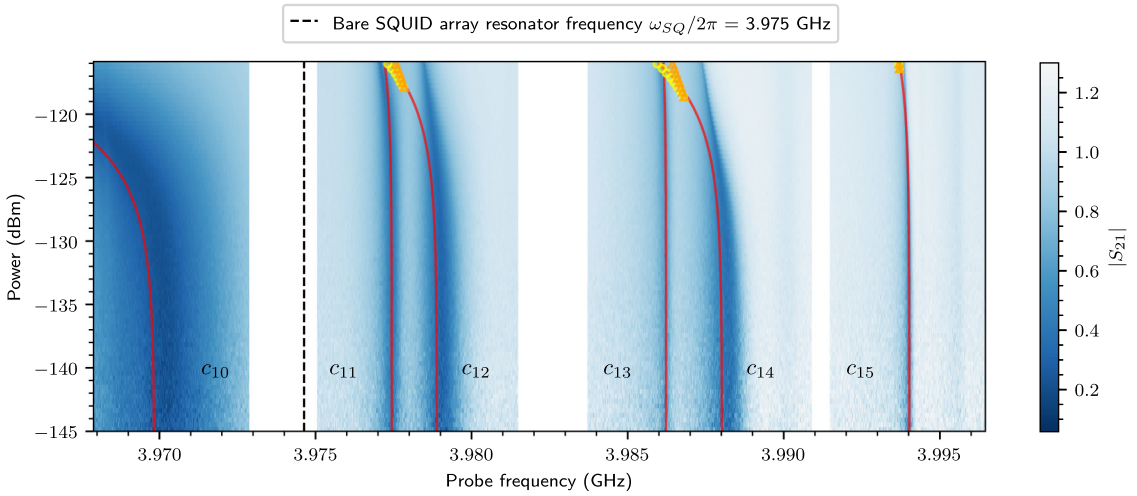


FIG. 22. Self-Kerr measurement at one flux value. Magnitude of the normalized transmission signal $|S_{21}|$ for increasing power of the probe tone. The measurement was performed around each hybrid modes individually. Red solid line shows the results of simulations for a driven classical Duffing resonator assuming the modes behave as independent oscillators. No extra fit parameters are used. The dashed black line marks the frequency of the bare SQUID array resonator ω_{SQ}. Yellow and orange markers show the region where each oscillator undergoes a bifurcation and enters a metastable region.

practice, the power of the pump tone is obtained by inverting Eq. (B20), where the frequency and dissipation rates of mode c_p as a function of ω_{SQ} are obtained from a fit of the S_{21} traces shown in Fig. 5(a) to Eq. (B18).

b. Analysis protocol

Here, to illustrate the protocol for analyzing two-tone spectroscopy maps, we focus on the pair of hybrid modes (c_{12}, c_p) . For each map in Figs. 23(b)–23(h), we extract the frequency of the probed mode c_{12} (yellow circles in Fig. 23 lower panel) as a function of the pump tone frequency, $\tilde{\omega}_{12}(f_{pump})$. To this end, we fit each S_{21} trace to the notch-type transmission signal Eq. (B18). However, because of impedance mismatch (or Fano interference), the line shape of some modes is distorted. This distortion induces a systematic offset between resonance frequency ω_r obtained from the fit to Eq. (B18) and the actual minimum in the magnitude of the measured S_{21} trace. This offset depends on the specific probed mode but is independent of the power applied to the pumped mode c_p. Therefore, to apply a uniform analysis protocol across the entire dataset, we use the minimum of the best-fit curve as the resonance frequency of the probed mode.

Subsequently, we extract the maximum negative displacement, $\Delta\tilde{\omega}^0_{12,p} := \Delta\tilde{\omega}^0_{12,p}(\bar{n}_p, \omega_{\mathrm{SQ}})$,

$$\Delta\tilde{\omega}^0_{12,p} = \min_{f_{pump}} \left(\tilde{\omega}_{12}(f_{pump})\right) - \tilde{\omega}^0_{12}, \tag{D7}$$

where $\tilde{\omega}^0_{12}/2\pi$ is the resonance frequency of the hybrid mode c_{12} from diagonalization of the linear model Eq. (B13). In addition, the number of excitations in the pumped mode $(\bar{n}_p)$ is recalibrated by using the frequency of the pump tone at maximum displacement $f_p^* = \arg\min_{f_{pump}} \left(\tilde{\omega}_{12}(f_{pump})\right)$.

The displacements, $\Delta\tilde{\omega}^0_{12,p}$, against the excitation number, $\bar{n}_p$, are then fitted to a linear model. The slope gives the cross-Kerr coefficient at the specific frequency of the SQUID array resonator considered, $\tilde{\chi}_{i,j}(\omega_{\mathrm{SQ}})$. The zero-order approximation for $\tilde{\omega}^0_{12}$ is provided by diagonalizing the linear model Eq. (B14). However, the required precision on the pump-off position of the probed modes would be below 10^{-5}. Therefore, in the linear fit we include the intercept as a fitting parameter. The dashed pink line in Fig. 23 is the pump-off frequency of the probed mode c_{12} obtained from the linear model corrected with the intercept from the fit: $\tilde{\omega}_{12} = \tilde{\omega}^0_{12} + \text{offset}$. By substituting the offset corrected frequency in Eq. (D7), we obtain $\Delta\tilde{\omega}_{12,p}$, shown in Fig. 5(c).

Finally, the uncertainty in the calibration of the line is the dominant source of error in the self- and cross-Kerr measurements, and it acts as a global rescaling of the Kerr coefficients. Therefore, we estimate its impact on the value of self-Kerr of the bare SQUID array resonator extracted from the fit as

$$\Delta\chi_{SQ,\pm} = \chi_{SQ} \times (10^{\pm\Delta\mathrm{A}/10} - 1), \tag{D8}$$

where ΔA is the uncertainty in the calibration of the SQUID array resonator feedline.

8. Two-photon drive measurements

Two-photon drives (also called parametric drives) are widely studied and can lead to bifurcation, bistability,

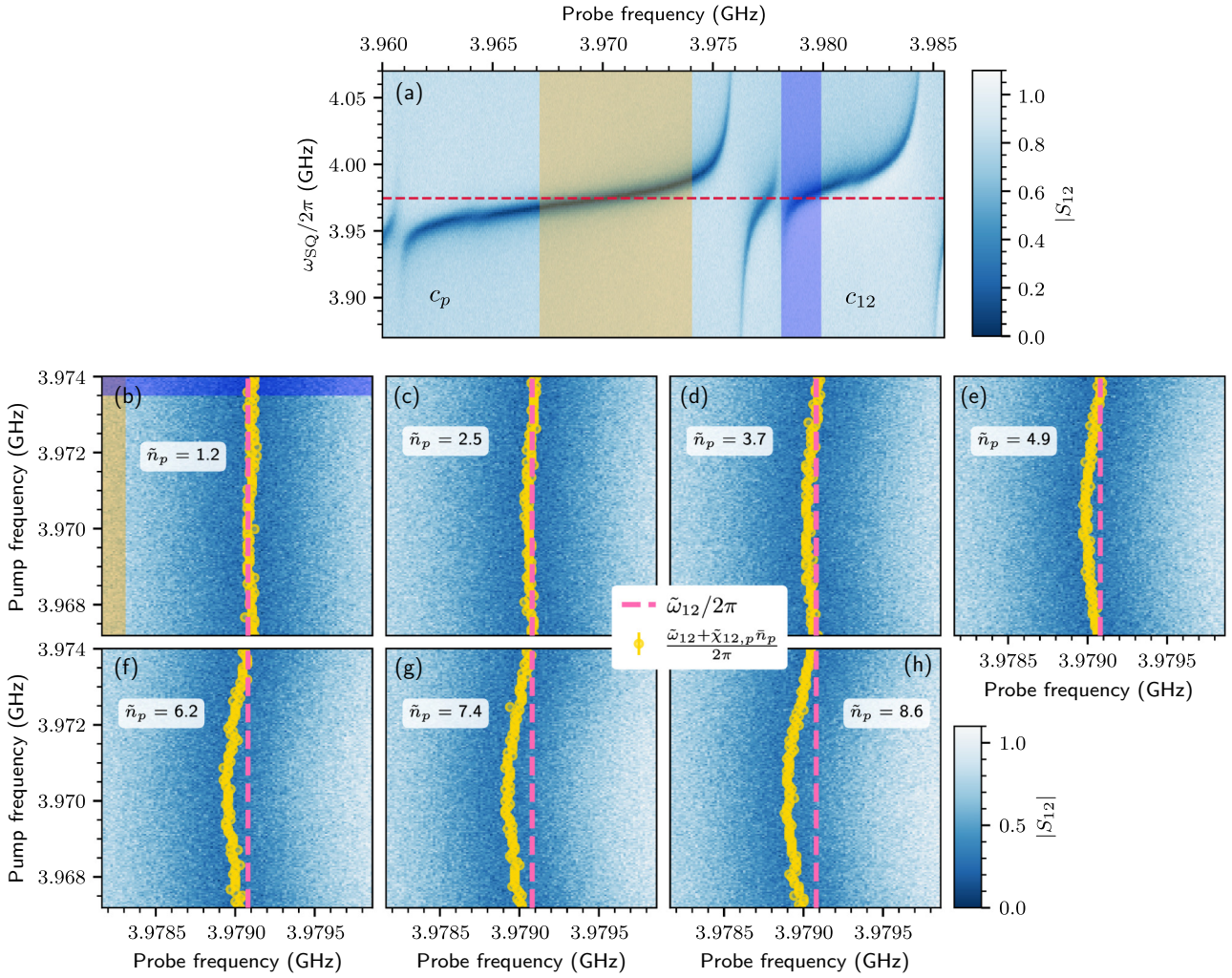


FIG. 23. Cross-Kerr measurement at one flux value. (a) Magnitude of the normalized transmission signal $|S_{21}|$ through the SQUID array resonators feedline as a function of the flux bias threading the SQUIDs loop. The dashed red line indicates the bare SQUID array resonator frequency ω_{SQ} in (b)–(h), while shaded regions highlight the frequency range of the pump tone on hybrid modes $c_p = \{c_8, c_9, c_{10}\}$ (orange) and of the probe tone on c_{12} (blue). (b)–(h) Power series of the two-tone spectroscopy maps of hybrid mode c_{12} while pumping the hybrid modes c_p. The pump power increases from left to right and from top to bottom. The shaded rectangles in (b) correspond to the shaded regions in the top panel. The dashed pink lines indicate the frequency of mode c_{12} in absence of pump tone, while the yellow circles mark the extracted resonance frequency of probed mode c_{12} for each pump frequency.

and amplification [100]. In this work we demonstrate that applying a drive at frequency $2\omega_p$ to the SQUID array flux line modulates its resonance frequency, leading to parametric down-conversion at ω_p in the SAW modes. This process is efficient when the SQUID array has a moderate detuning from the SAW modes, i.e., $\Delta \approx 1 - 10\,g$. Owing to the multimode regime, the SQUID array participation remains below a few percent in the hybrid modes, such that the downconverted excitations are mostly acoustic.

The bare SQUID array frequency is set to $\omega_{SQ}/2\pi = 3.965$ GHz. A microwave drive at frequency $2\omega_p$, close to twice a SAW mode frequency, is applied to the on-chip flux line (see Fig. 1). The applied power at room temperature is approximately -15 dBm. After waiting 500 µs, we collect the signal emitted from the launcher IDT (port 3). The signal quadratures I and Q are integrated over 15 µs and demodulated at ω_p, i.e., half the pump frequency. For the parameters used in Fig. 6, this integration time is much shorter than the typical switching time between metastable states, which is of order 10 ms. While keeping the $2\omega_p$ drive on, we collect between 1×10^5 [Fig. 6(a)] and 1.7×10^6 [Figs. 6(b) and 6(c)] data points. A short delay of 3 µs is inserted between two measurements to allow smooth data transfer without saturating the data buffer. The phase of the measured quadratures is shifted such that all the information lies along the I quadrature.

Measurements of I and Q quadratures over time are shown in Fig. 6(b) for one value of two-photon drive

strength and frequency. For five pump frequency values, we construct 2D histograms of the I and Q quadratures, shown in Fig. 6(c).

We also compute the steady-state phonon number $\tilde{n}$ as $\tilde{n} = \langle I^2 + Q^2 \rangle$, where the average is taken over each time trace. The steady-state phonon number is reported in Fig. 6(a) as a function of demodulation frequency ω_p. The phonon number is reported in arbitrary units as the precise calibration of the effective gain of the output line was not performed for this measurement.

In Fig. 6 we report signal down-conversion and nonlinear parametric instability for a single hybrid mode. However, when sweeping the parametric drive frequency $2\omega_p$, we observe similar parametric effects for several hybrid modes. For a given bare SQUID array frequency, mostly hybrid modes with frequencies below the SQUID array frequency display strong parametric response. This asymmetric behavior may be caused by the negative Kerr nonlinearity of the SQUID array. A thorough study of multimode parametric instabilities is left for future studies.

[1] S. Barzanjeh, A. Xuereb, S. Gröblacher, M. Paternostro, C. A. Regal, and E. M. Weig, Optomechanics for quantum technologies, Nat. Phys. **18**, 15 (2022).

[2] B. P. Abbott, R. Abbott, T. D. Abbott, M. R. Abernathy, F. Acernese, K. Ackley, C. Adams, T. Adams, P. Addesso, R. X. Adhikari *et al.*, Observation of gravitational waves from a binary black hole merger, Phys. Rev. Lett. **116**, 061102 (2016).

[3] M. V. Gustafsson, T. Aref, A. F. Kockum, M. K. Ekström, G. Johansson, and P. Delsing, Propagating phonons coupled to an artificial atom, Science **346**, 207 (2014).

[4] G. Andersson, B. Suri, L. Guo, T. Aref, and P. Delsing, Non-exponential decay of a giant artificial atom, Nat. Phys. **15**, 1123 (2019).

[5] M. Poot and H. S. van der Zant, Mechanical systems in the quantum regime, Phys. Rep. **511**, 273 (2012).

[6] A. Clerk, K. Lehnert, P. Bertet, J. Petta, and Y. Nakamura, Hybrid quantum systems with circuit quantum electrodynamics, Nat. Phys. **16**, 257 (2020).

[7] A. Ashkin, J. M. Dziedzic, J. E. Bjorkholm, and S. Chu, Observation of a single-beam gradient force optical trap for dielectric particles, Opt. Lett. **11**, 288 (1986).

[8] W. D. Phillips and H. Metcalf, Laser deceleration of an atomic beam, Phys. Rev. Lett. **48**, 596 (1982).

[9] A. D. O'Connell, M. Hofheinz, M. Ansmann, R. C. Bialczak, M. Lenander, E. Lucero, M. Neeley, D. Sank, H. Wang, M. Weides *et al.*, Quantum ground state and single-phonon control of a mechanical resonator, Nature **464**, 697 (2010).

[10] P. Arrangoiz-Arriola, E. A. Wollack, M. Pechal, J. D. Witmer, J. T. Hill, and A. H. Safavi-Naeini, Coupling a superconducting quantum circuit to a phononic crystal defect cavity, Phys. Rev. X **8**, 031007 (2018).

[11] J. D. Teufel, T. Donner, D. Li, J. W. Harlow, M. Allman, K. Cicak, A. J. Sirois, J. D. Whittaker, K. W. Lehnert, and R. W. Simmonds, Sideband cooling of micromechanical motion to the quantum ground state, Nature **475**, 359 (2011).

[12] S. Kotler, G. A. Peterson, E. Shojaee, F. Lecocq, K. Cicak, A. Kwiatkowski, S. Geller, S. Glancy, E. Knill, R. W. Simmonds *et al.*, Direct observation of deterministic macroscopic entanglement, Science **372**, 622 (2021).

[13] Y. Chu, P. Kharel, W. H. Renninger, L. D. Burkhart, L. Frunzio, P. T. Rakich, and R. J. Schoelkopf, Quantum acoustics with superconducting qubits, Science **358**, 199 (2017).

[14] R. Manenti, A. F. Kockum, A. Patterson, T. Behrle, J. Rahamim, G. Tancredi, F. Nori, and P. J. Leek, Circuit quantum acoustodynamics with surface acoustic waves, Nat. Commun. **8**, 975 (2017).

[15] K. J. Satzinger, Y. Zhong, H.-S. Chang, G. A. Peairs, A. Bienfait, M.-H. Chou, A. Cleland, C. R. Conner, É. Dumur, J. Grebel *et al.*, Quantum control of surface acoustic-wave phonons, Nature **563**, 661 (2018).

[16] L. R. Sletten, B. A. Moores, J. J. Viennot, and K. W. Lehnert, Resolving phonon Fock states in a multimode cavity with a double-slit qubit, Phys. Rev. X **9**, 021056 (2019).

[17] A. Noguchi, R. Yamazaki, Y. Tabuchi, and Y. Nakamura, Qubit-assisted transduction for a detection of surface acoustic waves near the quantum limit, Phys. Rev. Lett. **119**, 180505 (2017).

[18] J. Chen, X. He, W. Gao, X. Liu, Z. Niu, K. Liu, W. Peng, Z. Wang, and Z.-R. Lin, On-chip integration and strong coupling between ScAlN thin-film surface acoustic wave resonators and superconducting qubits, Appl. Phys. Lett. **126**, 144001 (2025).

[19] A. Hugot, Q. Greffe, G. Julie, E. Eyraud, F. Balestro, and J. Viennot, Approaching optimal microwave-acoustic transduction on lithium niobate using SQUID arrays, Nat. Electron. **9**, 152 (2026).

[20] E. E. Wollman, C. Lei, A. Weinstein, J. Suh, A. Kronwald, F. Marquardt, A. A. Clerk, and K. Schwab, Quantum squeezing of motion in a mechanical resonator, Science **349**, 952 (2015).

[21] S. Marti, U. von Lüpke, O. Joshi, Y. Yang, M. Bild, A. Omahen, Y. Chu, and M. Fadel, Quantum squeezing in a nonlinear mechanical oscillator, Nat. Phys. **20**, 1448 (2024).

[22] Y. Chu, P. Kharel, T. Yoon, L. Frunzio, P. T. Rakich, and R. J. Schoelkopf, Creation and control of multi-phonon Fock states in a bulk acoustic-wave resonator, Nature **563**, 666 (2018).

[23] H. Qiao, É. Dumur, G. Andersson, H. Yan, M.-H. Chou, J. Grebel, C. R. Conner, Y. J. Joshi, J. M. Miller, R. G. Povey *et al.*, Splitting phonons: Building a platform for linear mechanical quantum computing, Science **380**, 1030 (2023).

[24] M. Bild, M. Fadel, Y. Yang, U. Von Lüpke, P. Martin, A. Bruno, and Y. Chu, Schrödinger cat states of a 16-microgram mechanical oscillator, Science **380**, 274 (2023).

[25] F. Pistolesi, A. N. Cleland, and A. Bachtold, Proposal for a nanomechanical qubit, Phys. Rev. X **11**, 031027 (2021).

[26] X. Han, C.-L. Zou, W. Fu, M. Xu, Y. Xu, and H. X. Tang, Superconducting cavity electromechanics: The realization

of an acoustic frequency comb at microwave frequencies, Phys. Rev. Lett. **129**, 107701 (2022).
[27] C. Samanta, S. De Bonis, C. Møller, R. Tormo-Queralt, W. Yang, C. Urgell, B. Stamenic, B. Thibeault, Y. Jin, D. Czaplewski *et al.*, Nonlinear nanomechanical resonators approaching the quantum ground state, Nat. Phys. **19**, 1340 (2023).
[28] G. Andersson, S. W. Jolin, M. Scigliuzzo, R. Borgani, M. O. Tholén, J. C. Rivera Hernández, V. Shumeiko, D. B. Haviland, and P. Delsing, Squeezing and multimode entanglement of surface acoustic wave phonons, PRX Quantum **3**, 010312 (2022).
[29] Y. Yang, I. Kladarić, M. Drimmer, U. von Lüpke, D. Lenterman, J. Bus, S. Marti, M. Fadel, and Y. Chu, A mechanical qubit, Science **386**, 783 (2024).
[30] R. G. Cortinas, Towards the generation of mechanical Kerr-cats: Awakening the perturbative quantum Moyal corrections to classical motion, New J. Phys. **26**, 023022 (2024).
[31] E. A. Wollack, A. Y. Cleland, R. G. Gruenke, Z. Wang, P. Arrangoiz-Arriola, and A. H. Safavi-Naeini, Quantum state preparation and tomography of entangled mechanical resonators, Nature **604**, 463 (2022).
[32] U. von Lüpke, I. C. Rodrigues, Y. Yang, M. Fadel, and Y. Chu, Engineering multimode interactions in circuit quantum acoustodynamics, Nat. Phys. **20**, 564 (2024).
[33] R. Manenti, M. J. Peterer, A. Nersisyan, E. B. Magnusson, A. Patterson, and P. J. Leek, Surface acoustic wave resonators in the quantum regime, Phys. Rev. B **93**, 041411(R) (2016).
[34] G. Andersson, A. L. O. Bilobran, M. Scigliuzzo, M. M. de Lima, J. H. Cole, and P. Delsing, Acoustic spectral hole-burning in a two-level system ensemble, npj Quantum Inf. **7**, 15 (2021).
[35] R. G. Gruenke-Freudenstein, E. Szakiel, G. P. Multani, T. Makihara, A. G. Hayden, A. Khalatpour, E. A. Wollack, A. Akoto-Yeboah, S. Salmani-Rezaie, and A. H. Safavi-Naeini, Surface and bulk two-level system losses in lithium niobate acoustic resonators, Phys. Rev. Appl. **23**, 064055 (2025).
[36] S. A. Tadesse and M. Li, Sub-optical wavelength acoustic wave modulation of integrated photonic resonators at microwave frequencies, Nat. Commun. **5**, 5402 (2014).
[37] J.-C. Beugnot, S. Lebrun, G. Pauliat, H. Maillotte, V. Laude, and T. Sylvestre, Brillouin light scattering from surface acoustic waves in a subwavelength-diameter optical fibre, Nat. Commun. **5**, 5242 (2014).
[38] A. Iyer, Y. P. Kandel, W. Xu, J. M. Nichol, and W. H. Renninger, Coherent optical coupling to surface acoustic wave devices, Nat. Commun. **15**, 3993 (2024).
[39] S. J. Whiteley, G. Wolfowicz, C. P. Anderson, A. Bourassa, H. Ma, M. Ye, G. Koolstra, K. J. Satzinger, M. V. Holt, F. J. Heremans *et al.*, Spin–phonon interactions in silicon carbide addressed by gaussian acoustics, Nat. Phys. **15**, 490 (2019).
[40] S. Maity, L. Shao, S. Bogdanović, S. Meesala, Y.-I. Sohn, N. Sinclair, B. Pingault, M. Chalupnik, C. Chia, L. Zheng *et al.*, Coherent acoustic control of a single silicon vacancy spin in diamond, Nat. Commun. **11**, 193 (2020).
[41] Y. Sato, Jason C. H. Chen, M. Hashisaka, K. Muraki, and T. Fujisawa, Two-electron double quantum dot coupled to coherent photon and phonon fields, Phys. Rev. B **96**, 115416 (2017).
[42] M. J. A. Schuetz, E. M. Kessler, G. Giedke, L. M. K. Vandersypen, M. D. Lukin, and J. I. Cirac, Universal quantum transducers based on surface acoustic waves, Phys. Rev. X **5**, 031031 (2015).
[43] D. Meiser and P. Meystre, Superstrong coupling regime of cavity quantum electrodynamics, Phys. Rev. A—At., Mol. Opt. Phys. **74**, 065801 (2006).
[44] N. M. Sundaresan, Y. Liu, D. Sadri, L. J. Szőcs, D. L. Underwood, M. Malekakhlagh, H. E. Türeci, and A. A. Houck, Beyond strong coupling in a multimode cavity, Phys. Rev. X **5**, 021035 (2015).
[45] B. A. Moores, L. R. Sletten, J. J. Viennot, and K. W. Lehnert, Cavity quantum acoustic device in the multimode strong coupling regime, Phys. Rev. Lett. **120**, 227701 (2018).
[46] J. Puertas Martínez, S. Léger, N. Gheeraert, R. Dassonneville, L. Planat, F. Foroughi, Y. Krupko, O. Buisson, C. Naud, W. Hasch-Guichard *et al.*, A tunable Josephson platform to explore many-body quantum optics in circuit-QED, npj Quantum Inf. **5**, 19 (2019).
[47] R. Kuzmin, N. Mehta, N. Grabon, R. Mencia, and V. E. Manucharyan, Superstrong coupling in circuit quantum electrodynamics, npj Quantum Inf. **5**, 20 (2019).
[48] Y. Y. Gao, B. J. Lester, Y. Zhang, C. Wang, S. Rosenblum, L. Frunzio, L. Jiang, S. M. Girvin, and R. J. Schoelkopf, Programmable interference between two microwave quantum memories, Phys. Rev. X **8**, 021073 (2018).
[49] W.-L. Ma, S. Puri, R. J. Schoelkopf, M. H. Devoret, S. M. Girvin, and L. Jiang, Quantum control of bosonic modes with superconducting circuits, Sci. Bull. **66**, 1789 (2021).
[50] L. Li, X. Ruan, S.-L. Zhao, B.-J. Chen, G.-H. Liang, Y. Liu, C.-L. Deng, W.-P. Yuan, J.-C. Song, Z.-H. Liu *et al.*, Quantum acoustics with superconducting qubits in the multimode transition-coupling regime, Phys. Rev. Appl. **24**, 064064 (2025).
[51] F. Lecocq, L. Ranzani, G. A. Peterson, K. Cicak, R. W. Simmonds, J. D. Teufel, and J. Aumentado, Nonreciprocal microwave signal processing with a field-programmable Josephson amplifier, Phys. Rev. Appl. **7**, 024028 (2017).
[52] N. E. Frattini, V. V Sivak, A. Lingenfelter, S. Shankar, and M. H. Devoret, Optimizing the nonlinearity and dissipation of a snail parametric amplifier for dynamic range, Phys. Rev. Appl. **10**, 054020 (2018).
[53] F. Minganti, A. Biella, N. Bartolo, and C. Ciuti, Spectral theory of Liouvillians for dissipative phase transitions, Phys. Rev. A **98**, 042118 (2018).
[54] G. Beaulieu, F. Minganti, S. Frasca, V. Savona, S. Felicetti, R. Di Candia, and P. Scarlino, Observation of first-and second-order dissipative phase transitions in a two-photon driven kerr resonator, Nat. Commun. **16**, 1954 (2025).
[55] G. Beaulieu, F. Minganti, S. Frasca, M. Scigliuzzo, S. Felicetti, R. Di Candia, and P. Scarlino, Criticality-enhanced quantum sensing with a parametric superconducting resonator, PRX Quantum **6**, 020301 (2025).

[56] G. Mihailescu, U. Alushi, R. Di Candia, S. Felicetti, and K. Gietka, Critical quantum sensing: A tutorial on parameter estimation near quantum phase transitions, arXiv:2510.02035.

[57] P. Roushan, C. Neill, A. Megrant, Y. Chen, R. Babbush, R. Barends, B. Campbell, Z. Chen, B. Chiaro, A. Dunsworth *et al.*, Chiral ground-state currents of interacting photons in a synthetic magnetic field, Nat. Phys. **13**, 146 (2017).

[58] J. Del Pino, J. J. Slim, and E. Verhagen, Non-Hermitian chiral phononics through optomechanically induced squeezing, Nature **606**, 82 (2022).

[59] D. Morgan, *Surface Acoustic Wave Filters: With Applications to Electronic Communications and Signal Processing* (Academic, Northampton, UK, 2010).

[60] M. Fisicaro, T. A. Steenbergen, Y. C. Doedes, K. Heeck, and W. Löffler, Imaging transverse modes in a gigahertz surface-acoustic-wave cavity, Phys. Rev. Appl. **23**, 014032 (2025).

[61] A. G. Del Maestro and M. J. Gingras, Quantum spin fluctuations in the dipolar Heisenberg-like rare earth pyrochlores, J. Phys.: Condens. Matter **16**, 3339 (2004).

[62] S. E. Nigg, H. Paik, B. Vlastakis, G. Kirchmair, S. Shankar, L. Frunzio, M. H. Devoret, R. J. Schoelkopf, and S. M. Girvin, Black-box superconducting circuit quantization, Phys. Rev. Lett. **108**, 240502 (2012).

[63] Z. K. Minev, Z. Leghtas, S. O. Mundhada, L. Christakis, I. M. Pop, and M. H. Devoret, Energy-participation quantization of Josephson circuits, npj Quantum Inf. **7**, 131 (2021).

[64] L. R. Sletten, *Quantum Acoustics with Multimode Surface Acoustic Wave Cavities*, Ph.D. thesis, University of Colorado at Boulder, 2021.

[65] J.-M. Raimond and S. Haroche, *Exploring the Quantum* (Oxford University, Oxford, UK, 2006), Vol. 82, p. 17.

[66] L. Peyruchat, F. Minganti, M. Scigliuzzo, F. Ferrari, V. Jouanny, F. Nori, V. Savona, and P. Scarlino, Landau–Zener without a qubit: Multiphoton sidebands interaction and signatures of dissipative quantum chaos, npj Quantum Inf. **11**, 62 (2025).

[67] M. A. Castellanos-Beltran, K. Irwin, G. Hilton, L. Vale, and K. Lehnert, Amplification and squeezing of quantum noise with a tunable Josephson metamaterial, Nat. Phys. **4**, 929 (2008).

[68] C. Eichler and A. Wallraff, Controlling the dynamic range of a Josephson parametric amplifier, EPJ Quantum Technol. **1**, 1 (2014).

[69] C. W. Sandbo Chang, C. Sabín, P. Forn-Díaz, F. Quijandría, A. M. Vadiraj, I. Nsanzineza, G. Johansson, and C. M. Wilson, Observation of three-photon spontaneous parametric down-conversion in a superconducting parametric cavity, Phys. Rev. X **10**, 011011 (2020).

[70] R. Di Candia, F. Minganti, K. Petrovnin, G. S. Paraoanu, and S. Felicetti, Critical parametric quantum sensing, npj Quantum Inf. **9**, 23 (2023).

[71] Y. Cai, X. Deng, L. Zhang, Z. Ni, J. Mai, P. Huang, P. Zheng, L. Hu, S. Liu, Y. Xu *et al.*, Quantum squeezing amplification with a weak Kerr nonlinear oscillator, Nat. Commun. **17**, 970 (2025).

[72] S. Puri, C. K. Andersen, A. L. Grimsmo, and A. Blais, Quantum annealing with all-to-all connected nonlinear oscillators, Nat. Commun. **8**, 15785 (2017).

[73] P. Álvarez, D. Pittilini, F. Miserocchi, S. Raamamurthy, G. Margiani, O. Ameye, J. Del Pino, O. Zilberberg, and A. Eichler, Biased Ising model using two coupled Kerr parametric oscillators with external force, Phys. Rev. Lett. **132**, 207401 (2024).

[74] Jimmy S. C. Hung, J. H. Busnaina, C. W. Sandbo Chang, A. M. Vadiraj, I. Nsanzineza, E. Solano, H. Alaeian, E. Rico, and C. M. Wilson, Quantum simulation of the bosonic Creutz ladder with a parametric cavity, Phys. Rev. Lett. **127**, 100503 (2021).

[75] J. J. Slim, J. del Pino, and E. Verhagen, Programmable synthetic magnetism and chiral edge states in nano-optomechanical quantum hall networks, Nat. Commun. **16**, 7471 (2025).

[76] L. Yuan, Q. Lin, M. Xiao, and S. Fan, Synthetic dimension in photonics, Optica **5**, 1396 (2018).

[77] T. Ozawa and H. M. Price, Topological quantum matter in synthetic dimensions, Nat. Rev. Phys. **1**, 349 (2019).

[78] M. Fitzpatrick, N. M. Sundaresan, Andy C. Y. Li, J. Koch, and A. A. Houck, Observation of a dissipative phase transition in a one-dimensional circuit QED lattice, Phys. Rev. X **7**, 011016 (2017).

[79] U. Alushi, A. Coppo, V. Brosco, R. Di Candia, and S. Felicetti, Collective quantum enhancement in critical quantum sensing, Commun. Phys. **8**, 74 (2025).

[80] F. Yilmaz, S. Singh, M. F. Zwanenburg, J. Hu, T. V. Stefanski, and C. K. Andersen, Energy participation ratio analysis for very anharmonic superconducting circuits, arXiv:2411.15039.

[81] J. Koch, T. M. Yu, J. Gambetta, A. A. Houck, D. I. Schuster, J. Majer, A. Blais, M. H. Devoret, S. M. Girvin, and R. J. Schoelkopf, Charge-insensitive qubit design derived from the Cooper pair box, Phys. Rev. A—At., Mol. Opt. Phys. **76**, 042319 (2007).

[82] M. Boissonneault, J. M. Gambetta, and A. Blais, Improved superconducting qubit readout by qubit-induced nonlinearities, Phys. Rev. Lett. **105**, 100504 (2010).

[83] S. Kono, J. Pan, M. Chegnizadeh, X. Wang, A. Youssefi, M. Scigliuzzo, and T. J. Kippenberg, Mechanically induced correlated errors on superconducting qubits with relaxation times exceeding 0.4 ms, Nat. Commun. **15**, 3950 (2024).

[84] I. Carusotto and C. Ciuti, Quantum fluids of light, Rev. Mod. Phys. **85**, 299 (2013).

[85] Y. Wang, J. Lee, and P. X.-L. Feng, Perspectives on phononic waveguides for on-chip classical and quantum transduction, Appl. Phys. Lett. **124**, 070502 (2024).

[86] M. Scigliuzzo, L. Peyruchat, R. M. Marabini, C. Becker, V. Jouanny, P. Delsing, and P. Scarlino, Data and code for the article "Quantum acoustics with tunable nonlinearity in the superstrong coupling regime", 2026, https://doi.org/10.5281/zenodo.18258484

[87] P. Politzer and J. S. Murray, The Hellmann-Feynman theorem: A perspective, J. Mol. Model. **24**, 1 (2018).

[88] Q.-M. Chen, M. Partanen, F. Fesquet, K. E. Honasoge, F. Kronowetter, Y. Nojiri, M. Renger, K. G. Fedorov, A. Marx, F. Deppe *et al.*, Scattering coefficients of

superconducting microwave resonators. II. System-bath approach, Phys. Rev. B **106**, 214506 (2022).

[89] S. Probst, F. Song, P. A. Bushev, A. V. Ustinov, and M. Weides, Efficient and robust analysis of complex scattering data under noise in microwave resonators, Rev. Sci. Instrum. **86**, 024706 (2015).

[90] A. Blais, A. L. Grimsmo, S. M. Girvin, and A. Wallraff, Circuit quantum electrodynamics, Rev. Mod. Phys. **93**, 025005 (2021).

[91] G. Kirchmair, B. Vlastakis, Z. Leghtas, S. E. Nigg, H. Paik, E. Ginossar, M. Mirrahimi, L. Frunzio, S. M. Girvin, and R. J. Schoelkopf, Observation of quantum state collapse and revival due to the single-photon Kerr effect, Nature **495**, 205 (2013).

[92] J. R. Johansson, P. D. Nation, and F. Nori, QuTiP: An open-source Python framework for the dynamics of open quantum systems, Comput. Phys. Commun. **183**, 1760 (2012).

[93] K. Satzinger, C. Conner, A. Bienfait, H.-S. Chang, M.-H. Chou, A. Cleland, É. Dumur, J. Grebel, G. Peairs, R. Povey *et al.*, Simple non-galvanic flip-chip integration method for hybrid quantum systems, Appl. Phys. Lett. **114**, 173501 (2019).

[94] C. Conner, A. Bienfait, H.-S. Chang, M.-H. Chou, É. Dumur, J. Grebel, G. Peairs, R. Povey, H. Yan, Y. Zhong *et al.*, Superconducting qubits in a flip-chip architecture, Appl. Phys. Lett. **118**, 232602 (2021).

[95] J. Kitzman, J. Lane, C. Undershute, P. Harrington, N. Beysengulov, C. Mikolas, K. Murch, and J. Pollanen, Phononic bath engineering of a superconducting qubit, Nat. Commun. **14**, 3910 (2023).

[96] G. Calajó, F. Ciccarello, D. Chang, and P. Rabl, Atom-field dressed states in slow-light waveguide QED, Phys. Rev. A **93**, 033833 (2016).

[97] T. Aref, P. Delsing, M. K. Ekström, A. F. Kockum, M. V. Gustafsson, G. Johansson, P. J. Leek, E. Magnusson, and R. Manenti, Quantum acoustics with surface acoustic waves, in *Superconducting devices in quantum optics* (Springer, 2016), p. 217.

[98] A. L. Emser, B. C. Rose, L. R. Sletten, P. Aramburu Sanchez, and K. W. Lehnert, Minimally diffracting quartz for ultra-low temperature surface acoustic wave resonators, Appl. Phys. Lett. **121**, 224001 (2022).

[99] P. R. Muppalla, O. Gargiulo, S. I. Mirzaei, B. P. Venkatesh, M. L. Juan, L. Grünhaupt, I. M. Pop, and G. Kirchmair, Bistability in a mesoscopic Josephson junction array resonator, Phys. Rev. B **97**, 024518 (2018).

[100] A. Eichler and O. Zilberberg, *Classical and Quantum Parametric Phenomena* (Oxford University, Oxford, UK, 2023).